



Mohamed A. Attia · Rabab A. Shanab

# Dynamic analysis of 2DFGM porous nanobeams under moving load with surface stress and microstructure effects using Ritz method

Received: 7 June 2023 / Revised: 4 August 2023 / Accepted: 12 August 2023 / Published online: 11 September 2023  
© The Author(s) 2023

**Abstract** This paper investigates the dynamic behavior of micro/nanobeams made of two-dimensional functionally graded porous material (2DFGPM) under accelerated, decelerated, and uniform moving harmonic load, using surface elasticity and modified couple stress theories. The key feature of this formulation is that it deals with a higher order shear deformation beam theory. The non-classical equilibrium equations are developed using Lagrange's equation and the concept of physical neutral surface. The equations of motion are derived using the same approach, accounting for the porosity effect and the modified power-law distribution of material properties. The trigonometric Ritz method is used with sinusoidal trial functions for the displacement field, and the Newmark method is applied to obtain the dynamical response of 2DFGPM nanobeams. The results are compared with previous studies, and the impact of critical parameters such as gradation indices, volume fraction ratio, pattern of porosity, velocity, frequency, and motion type of the applied force are explored. This study highlights the importance of considering the porosity effect, as neglecting it can lead to significant errors in the predicted results. Additionally, the study found that the accelerated and decelerated motions of the applied load have a greater impact on the dynamical deflection of 2DFGPM nanobeams than the uniform motion. The findings of this study can provide guidance for the optimal design of micro/nanobeams subjected to a moving force with multifunctional properties.

## 1 Introduction

Functionally graded materials (FGMs) are composite materials composed of two or more distinct materials with specific gradients leading to a desired continuous change of their properties in specific spatial direction(s). FGMs can provide advantages such as higher strength, higher stiffness, higher thermal resistance, higher corrosion resistance, and elimination of residual stresses and interlaminar shear stress [1, 2]. The distinctive properties of FGMs make them highly sought after as structural components in a wide range of engineering disciplines, including nuclear, aerospace, automotive, marine, biomedical, and optical engineering, leading to their rapid adoption [3]. As a consequence, numerous studies have been performed using analytical, semi-analytical, and numerical techniques to explore the mechanical behavior of unidimensional FGM (UDFGM) structures, such as transversely FGM (TFGM) and axially FGM (AFGM), along with the thickness and length directions, respectively, (see in Refs. [4–11]).

In the last decades, the design and investigation of nanomaterials and nanostructures have been extensively increased due to their superior mechanical, thermal, and electrical properties. Nanostructures like beams, shells,

---

M. A. Attia  
Department of Mechanical Design and Production Engineering, Faculty of Engineering, Zagazig University, Zagazig 44519, Egypt

R. A. Shanab (✉)  
Engineering Mathematics Department, Faculty of Engineering, Zagazig University, Zagazig 44519, Egypt  
e-mail: rabab\_shanab@yahoo.com; rabab\_shanab@zu.edu.eg

rods, and plates at the nanoscale have been recently used in numerous applications in micro/ nanoscale devices such as sensors and actuators. Since the classical continuum mechanics theory (CLCMT) is size-independent, it cannot capture the size effect on the behavior of micro/nanostructures [12–16]. In this regard, molecular dynamic approaches and size-dependent continuum mechanics theories are employed to incorporate the effect of small-scale in micro/ and nanostructures [17, 18]. However, numerical simulations using molecular dynamic approaches are generally complex and computationally expensive, especially for complicated structures. Thus, several non-classical continuum mechanics theories (NCCMTs), including additional material length scale parameters (MLSPs), have been proposed to model the size-dependent phenomenon in miniaturized systems. Critical reviews on the modeling of micro/nanostructures based on different NCCMTs have been presented by [19, 20].

The determination of the microstructural MLSPs is the most challenging aspect of the NCCMTs. The modified couple stress theory (MCST) proposed by Yang et al. [21] has the advantage of involving only one additional MLSP for isotropic materials. In the present study, the MCST is adapted to include the impact of microstructure on the predicted response. Moreover, for a large ratio of surface area to bulk volume, the free energy of surface atoms becomes comparable to that of the bulk part, and thus, the surface energy has a crucial influence on the characteristics and behavior of small-scale structures. The Gurtin–Murdoch surface elasticity theory (GM-SET) [22, 23] has been successfully employed in the analysis of homogeneous and FGM structures.

The functionally graded porous materials (FGPMs) are used in many industrial fields to fabricate lightweight structures with high stiffness. The performance of micro/nanostructures can be controlled by setting artificial porosities inside the structure, such as electronic devices, sensors, and solar cells [24]. Also, the voids and porosities cannot be avoided in the continuum because of the technical problems encountered in the fabrication of FGMs leading to reduced strength. Thus, several works have been performed to explore the mechanical behavior of FGPM micro/nanobeams [25–33], plates, [34–41], shells [42], and sandwich structures [43]

Structures and components in advanced machines require advanced composites with continuously varying properties in more than one direction to satisfy the requirements of temperature and stress distributions in two or more directions, Nemat-Alla [44]. With the rapid advancement in nanomechanics, the mechanics of 2DFGM micro/nanosized beams have been explored using the MCST [45–51], differential nonlocal elasticity theory (DNET) [52–55], and differential nonlocal strain gradient theory (DNSGT) [56–61]. However, considering the surface effect on 2DFGM nanobeams, only a few models have been recently developed. Adopting the GM-SET with DNET, the vibration of Power law 2DFGM Timoshenko nanobeam was studied by Lal & Dangi [62] using the differential quadrature method (DQM). The surface constants were graded in the transverse direction only and a constant nonlocal parameter was assumed, which means an inconsistent gradation of the material constants. An extensively studied the mechanics of 2DFGM Euler–Bernoulli and Timoshenko micro/nanobeams using MCST and GM-SET [63–65]. In these studies, and unlike [62], all the bulk and surface material constants were graded in both the transverse and longitudinal directions via a power law.

Analyzing structures' response under moving mass/load is essential for many practical engineering applications, such as bridges, tunnels, and rail. The vibration problems of a homogenous beam due to a moving load were extensively studied in [66–69]. The dynamical performance of a moving force was studied by [70–73] for TFGM beams and [74–76] for AFGM beams. Considering the features of 2DFGM, the free and forced vibrations of exponential 2DFGM beams under a moving force were explored by Simsek [77] using Ritz and the implicit time integration methods. Nguyen et al. [78] utilized the finite element method (FEM) and Newmark method to study the dynamics of a moving force of a power-law 2DFGM Timoshenko beam. Yang et al. [79] explored the vibration to a moving load of an exponential 2DFGM tapered Timoshenko beam employing the meshfree boundary-domain integral equation together with the 2D elasticity theory. Employing the Ritz method and Gram-Schmidt orthogonalization procedure, FG graphene nanoplatelet-reinforced beam dynamics acted by multiple moving loads based on third-order shear deformation beam theory (SDBT) was explored by [80]. Recently, Nguyen et al. [81] utilized FEM and Newmark method to study the response of a sandwich Timoshenko beam with power-law 2DFGM face layers due to a moving load. This work was extended by Vu et al. [82] to investigate the response of 2DFGM sandwich beams resting on a partial elastic foundation via a quasi-3D theory. The effects of centrifugal and Coriolis forces on the dynamics of inclined 2DFGM sandwich beams using SDBT were presented by Nguyen et al. [83]. For the double-2DFGM porous beam system, the vibration performance to moving load was studied by Chen et al. [84], adopting Ritz and Newmark methods.

Including the scale-effect phenomena of micro/nanoscale beams acted by moving loads, Hosseini & Rahmani [85] studied the dynamics of simply-supported TFGM Euler–Bernoulli nanobeams under a constant moving force utilizing the DNET. Adopting the DNET and GM-SET, the effects of a viscoelastic foundation

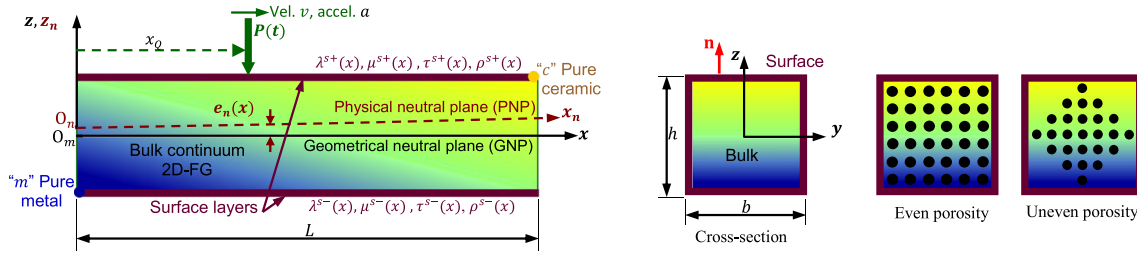


**Fig. 1** Sketch of a 2DFGM nanobeam with surface layers exposed to a moving load with even and uneven porosity distributions

on the steady-state response of Euler–Bernoulli nanobeam due to a thermal environment and a moving force were examined by Ghadiri et al. [86] using the multiple scales method. In Barati & Shahverdi [87], vibration to a uniform moving load of TFGM nanobeams in an elastic medium was investigated using DNET. Adopting the NSGT, the dynamical performance of a moving force of TFGM nanobeams was studied by Babaei [88] and Esen et al. [89]. Regarding 2DFGM nanobeams, Rajasekaran and Khaniki [90] used the MCST to study the vibration of 2DFGM nonuniform microbeams, with different gradation schemes, resting on an elastic foundation and acted by a moving force/mass using the FEM and Wilson-theta method. Zhang and Liu [91] employed the MCST to examine the vibration of power-law 2DFGM porous Reddy microbeams excited by a moving force. Based on the MCST, Liu et al. [92] used FEM to study the dynamics of power-law 2DFGM microbeams under a temperature rise and a moving force. Recently, Attia et al. [93] developed a closed-form solution using Laplace transform to study the dynamic response of sigmoid 2DFGM microbeams under moving harmonic load and thermal environmental conditions for a simply-supported boundary condition. Adopting the MCST and GM-SET, the dynamical performance of a moving load of perfect 2DFGM nanobeams was studied by Attia and Shanab [94].

The main objective of the present study is to develop an integrated microstructure-surface energy-based model for predicting the size-dependent dynamical response of porous 2DFGM nanobeams under accelerated, decelerated, and uniform moving load based on a higher-order shear deformation beam theory for the first time. Towards this end, GM-SET and MCST are adopted to capture the contributions of the surface energy and microstructure, respectively. The modified power-law function is adopted to express the gradation in both transverse and longitudinal directions for all the material properties of the bulk and surface layers. Both even and uneven distribution patterns of porosity are presented. Considering Poisson’s effect and the physical neutral axis concept, Lagrange’s equation is exploited to derive the non-classical governing equations. Trigonometric Ritz and Newmark methods are applied to obtain the dynamical response of 2DFGM nanobeam under a moving load with uniform, accelerated, and decelerated motions. For verification purposes, the predicted results are compared with the previous studies. Numerical studies proved the significant influence of the gradation indices, volume fraction ratio, and distribution pattern of porosity, moving velocity, motion type, and frequency of the moving load, microstructure, and surface energy on the dynamic response of 2DFGM nanobeams.

## 2 Mathematical formulation

Consider a straight uniform 2DFGM beam with length  $L$ , width  $b$ , and thickness  $h$ , as demonstrated in Fig. 1, in a Cartesian coordinate system  $(x, y, z)$  that denotes the geometrical neutral plane (midplane). The beam is excited by a moving harmonic load with a velocity  $v$  and an acceleration  $a$ . The beam is composed of a mixture of ceramic “c” and metallic “m” constituents, where the lowermost ( $x = 0, z = -h/2$ ) and uppermost ( $x = L, z = h/2$ ) surfaces of the nanobeam are pure metal and pure ceramic, respectively.

Including the porosity effect, the material properties describing the bulk and surface continuums of 2DFGPM nanobeam can be expressed via a modified power-law in both length and thickness directions [49, 90]. For even distribution of porosity:

$$\begin{Bmatrix} E^B(x, z) \\ \nu(x, z) \\ \rho^B(x, z) \end{Bmatrix} = \begin{Bmatrix} E_c^B - E_m^B \\ \nu_c - \nu_m \\ \rho_c^B - \rho_m^B \end{Bmatrix} \left[ \left( \frac{x}{L} \right)^{k_x} \left( \frac{1}{2} + \frac{z}{h} \right)^{k_z} \right] + \begin{Bmatrix} E_m^B \\ \nu_m \\ \rho_m^B \end{Bmatrix} - \frac{\alpha}{2} \begin{Bmatrix} E_c^B + E_m^B \\ \nu_c + \nu_m \\ \rho_c^B + \rho_m^B \end{Bmatrix} \quad (1)$$

$$l(x, z) = (l_c - l_m) \left[ \left( \frac{x}{L} \right)^{k_x} \left( \frac{1}{2} + \frac{z}{h} \right)^{k_z} \right] + l_m - \frac{\alpha}{2} (l_c + l_m) \quad (2)$$

$$\begin{Bmatrix} \tau^s(x, z) \\ \lambda^s(x, z) \\ \mu^s(x, z) \\ \rho^s(x, z) \end{Bmatrix} = \begin{Bmatrix} \tau_c^s - \tau_m^s \\ \lambda_c^s - \lambda_m^s \\ \mu_c^s - \mu_m^s \\ \rho_c^s - \rho_m^s \end{Bmatrix} \left[ \left( \frac{x}{L} \right)^{k_x} \left( \frac{1}{2} + \frac{z}{h} \right)^{k_z} \right] + \begin{Bmatrix} \tau_m^s \\ \lambda_m^s \\ \mu_m^s \\ \rho_m^s \end{Bmatrix} - \frac{\alpha}{2} \begin{Bmatrix} \tau_c^s + \tau_m^s \\ \lambda_c^s + \lambda_m^s \\ \mu_c^s + \mu_m^s \\ \rho_c^s + \rho_m^s \end{Bmatrix} \quad (3)$$

and for uneven distribution of porosity:

$$\begin{Bmatrix} E^B(x, z) \\ \nu(x, z) \\ \rho^B(x, z) \end{Bmatrix} = \begin{Bmatrix} E_c^B - E_m^B \\ \nu_c - \nu_m \\ \rho_c^B - \rho_m^B \end{Bmatrix} \left[ \left( \frac{x}{L} \right)^{k_x} \left( \frac{1}{2} + \frac{z}{h} \right)^{k_z} \right] + \begin{Bmatrix} E_m^B \\ \nu_m \\ \rho_m^B \end{Bmatrix} - \frac{\alpha}{2} \left( 1 - 2 \frac{|z|}{h} \right) \begin{Bmatrix} E_c^B + E_m^B \\ \nu_c + \nu_m \\ \rho_c^B + \rho_m^B \end{Bmatrix} \quad (4)$$

$$l(x, z) = (l_c - l_m) \left[ \left( \frac{x}{L} \right)^{k_x} \left( \frac{1}{2} + \frac{z}{h} \right)^{k_z} \right] + l_m - \frac{\alpha}{2} \left( 1 - 2 \frac{|z|}{h} \right) (l_c + l_m) \quad (5)$$

$$\begin{Bmatrix} \tau^s(x, z) \\ \lambda^s(x, z) \\ \mu^s(x, z) \\ \rho^s(x, z) \end{Bmatrix} = \begin{Bmatrix} \tau_c^s - \tau_m^s \\ \lambda_c^s - \lambda_m^s \\ \mu_c^s - \mu_m^s \\ \rho_c^s - \rho_m^s \end{Bmatrix} \left[ \left( \frac{x}{L} \right)^{k_x} \left( \frac{1}{2} + \frac{z}{h} \right)^{k_z} \right] + \begin{Bmatrix} \tau_m^s \\ \lambda_m^s \\ \mu_m^s \\ \rho_m^s \end{Bmatrix} - \frac{\alpha}{2} \left( 1 - 2 \frac{|z|}{h} \right) \begin{Bmatrix} \tau_c^s + \tau_m^s \\ \lambda_c^s + \lambda_m^s \\ \mu_c^s + \mu_m^s \\ \rho_c^s + \rho_m^s \end{Bmatrix} \quad (6)$$

where the superscripts “s” and “B” denotes, respectively, to the surface layers and the bulk of the beam. The bulk parameters are  $E$ ,  $\nu$ , and  $\rho$ , which denote Young’s modulus, Poisson’s ratio, and the mass density, respectively. The surface parameters are residual stress  $\tau^s$ , elastic constants  $\lambda^s$ ,  $\mu^s$ , and the mass density  $\rho^s$ .  $l$  is the MLSP capturing the influence of microstructure on the beam bulk.  $k_x$  and  $k_z$  are the power law gradation indices in the longitudinal and transverse directions, respectively. For even and uneven porosities,  $\alpha$  denotes the porosity volume fraction ratio.

In Eqs. (1–6), one can recover the distributions of porous AFGM and TFGM by setting  $k_z = 0$ ,  $k_x \neq 0$  and  $k_x = 0$ ,  $k_z \neq 0$ , respectively. A homogeneous pure ceramic beam is obtained when  $k_x = k_z = 0$ . Also, for a perfect material, the porosity ratio  $\alpha = 0$ .

The physical neutral plane (PNP) of a 2DFGPM beam deviates from the geometrical neutral plane due to the nonsymmetric distribution of its elastic properties about the midplane (GNP), as demonstrated in Fig. 1. The deviation  $e_n(x)$  between the positions of GNP and PNP is given by [49, 63]

$$e_n(x) = \frac{\int_{-h/2}^{h/2} \int_{-b/2}^{b/2} z [\lambda^B(x, z) + 2\mu^B(x, z)] dy dz}{\int_{-h/2}^{h/2} \int_{-b/2}^{b/2} [\lambda^B(x, z) + 2\mu^B(x, z)] dy dz}, \quad z_n(x) = z - e_n(x) \quad (7)$$

where  $\lambda^B$  and  $\mu^B$  are the classical Lamé’s constants of the bulk material,

$$\lambda^B(x, z) = \frac{E^B(x, z)\nu(x, z)}{(1 + \nu(x, z))(1 - 2\nu(x, z))} \quad \text{and} \quad \mu^B(x, z) = \frac{E^B(x, z)}{2(1 + \nu(x, z))} \quad (8)$$

Ignoring the Poisson’s effect yields  $[\lambda^B(x, z) + 2\mu^B(x, z)] \equiv E^B(x, z)$  as adopted in [56, 57, 91].

From Eq. (7), it is observed that the deviation  $e_n$  in a 2DFGPM beam depends on the  $x$ -coordinate. For simplicity, we used the Cartesian coordinates to approximate the  $z_n$ -coordinate instead of the curvilinear coordinates.

## 2.1 Kinematics and constitutive relations

In this study, a general higher-order shear deformation theory is used to express the kinematics of the 2DFGPM nanobeam, in which the displacement field is

$$u_x(x, z, t) = u(x) + f(z_n) \frac{\partial w(x, t)}{\partial x} + R(z_n) \phi(x, t), \quad u_y(x, z, t) = 0, \quad u_z(x, z, t) = w(x, t) \quad (9)$$

where  $u$  and  $w$  are the axial and transverse displacements at the midplane in  $x$  and  $z$  directions, respectively,  $\phi$  is the transverse shear strain, and  $t$  denotes time. Accounting for the PNP concept, the shear-strain function is given by

$$r_n(x) = \frac{\int_{-h/2}^{h/2} \int_{-b/2}^{b/2} R(z) [\lambda^B(x, z) + 2\mu^B(x, z)] dy dz}{\int_{-h/2}^{h/2} \int_{-b/2}^{b/2} [\lambda^B(x, z) + 2\mu^B(x, z)] dy dz}, \quad R(z_n) = R(z) - r_n(x) \quad (10)$$

Various beam theories can be satisfied by an appropriate selection of the functions  $f(z_n)$  and  $R(z_n)$ . Adopting the third-order parabolic shear deformable beam theory (PSDBT) [95]

$$f(z_n) = -z_n \quad \text{and} \quad R(z_n) = z_n - \frac{4z_n^3}{3h^2} \quad (11)$$

In the framework of the generalized elasticity theory in combination with the MCST, Yang et al. [21], the infinitesimal green strain tensor  $\boldsymbol{\varepsilon}$ , classical Cauchy stress tensor  $\boldsymbol{\sigma}^B$ , symmetric curvature tensor  $\boldsymbol{\chi}$ , and the deviatoric part of the couple stress tensor  $\boldsymbol{m}$  are given by [96, 97]

$$\boldsymbol{\varepsilon} = \frac{1}{2} [\nabla \mathbf{u} + (\nabla \mathbf{u})^T] \quad (12a)$$

$$\boldsymbol{\sigma}^B = \lambda^B(x, z) \text{tr}(\boldsymbol{\varepsilon}) \mathbf{I} + 2\mu^B(x, z) \boldsymbol{\varepsilon} \quad (12b)$$

$$\boldsymbol{\chi} = \frac{1}{2} [\nabla \boldsymbol{\theta} + (\nabla \boldsymbol{\theta})^T], \quad \boldsymbol{\theta} = \frac{1}{2} \text{curl}(\mathbf{u}) \quad (13a)$$

$$\boldsymbol{m} = [2l^2(x, z) \mu^B(x, z)] \boldsymbol{\chi} \quad (13b)$$

where  $\mathbf{u}$  and  $\boldsymbol{\theta}$  represent the vectors of the displacement and rotation fields, respectively. In this study, the gradation of the MLSP in the longitudinal and transverse directions is considered including the porosity effect, Eqs. (2, 4).

According to the GM-SET [22, 23], the surface layer of bulk material is of zero thickness and fulfills different constitutive equations involving the surface parameters, i.e., residual surface stress  $\tau^s$  and the surface elastic constants  $\lambda^s$  and  $\mu^s$ . In this theory, the in-plane ( $\boldsymbol{\sigma}^s$ ) and out-of-plane ( $\boldsymbol{\sigma}_{n\alpha}^s$ ) surface stress tensors are given as follows, respectively, [22, 23]

$$\boldsymbol{\sigma}^{s\pm} = 2[\mu^{s\pm}(x) - \tau^{s\pm}(x)] \boldsymbol{\varepsilon}^{\pm} + [\tau^{s\pm}(x) + [\lambda^{s\pm}(x) + \tau^{s\pm}(x)] \text{tr}(\boldsymbol{\varepsilon}^{\pm})] \mathbf{I} + \tau^{s\pm}(x) \nabla^s \mathbf{u}^{\pm} \quad (14a)$$

$$\boldsymbol{\sigma}_{n\alpha}^{s\pm} = \tau^{s\pm}(x) u_{n,\alpha}^{\pm}, \quad \alpha = 1, 2 \quad (14b)$$

In Eqs. (14), the signs (+) and (−) stand for the upper and lower surface layers of the 2DFGPM beam at  $z = +h/2$  and  $z = -h/2$ , respectively.  $n_i$  denotes the components of the outward unit normal vector  $\mathbf{n}$  to the beam lateral surface.

The nonzero components of the strain and the symmetric curvature tensors can be obtained using Eqs. (9), (11), (12a), and (13a) as

$$\varepsilon_{xx} = \frac{\partial u}{\partial x} - z_n \frac{\partial^2 w}{\partial x^2} + R(z_n) \frac{\partial \phi}{\partial x}, \quad \gamma_{xz} = \gamma_{zx} = 2\varepsilon_{xz} = \frac{\partial R(z_n)}{\partial z_n} \phi \quad (15)$$

$$\chi_{xy} = \chi_{yx} = \frac{1}{2} \left( \frac{1}{2} \frac{\partial R(z_n)}{\partial z_n} \frac{\partial \phi}{\partial x} - \frac{\partial^2 w}{\partial x^2} \right), \quad \chi_{yz} = \chi_{zy} = \frac{1}{4} \frac{\partial^2 R(z_n)}{\partial z_n^2} \phi \quad (16)$$

In light of Eqs. (12b) and (13b), the nonzero components of the classical stress and the deviatoric part of the couple stress tensors are [64, 65]

$$\sigma_{xx}^B = \mathbb{E}^B(x, z) \varepsilon_{xx}, \quad \sigma_{xz}^B = \mu^B(x, z) \frac{\partial R(z_n)}{\partial z_n} \phi; \quad \mathbb{E}^B(x, z) = [\lambda^B(x, z) + 2\mu^B(x, z)] \quad (17)$$

$$m_{yx} = m_{xy} = 2\mathbb{Q}(x, z)\chi_{xy}, \quad m_{zy} = m_{yz} = 2\mathbb{Q}(x, z)\chi_{zy}; \quad \mathbb{Q}(x, z) = l^2(x, z)\mu^B(x, z) \quad (18)$$

The surface stresses are obtained by substituting Eqs. (9) and (15) into Eqs. (14),

$$\begin{aligned} \sigma_{xx}^{s\pm} &= \tau^{s\pm}(x) + \mathbb{F}^{s\pm}(x)\varepsilon_{xx}^\pm; \quad \mathbb{F}^{s\pm}(x) = \lambda^{s\pm}(x) + 2\mu^{s\pm}(x) \\ \sigma_{xf}^{s\pm} &= \left[ 2\mu^{s\pm}(x)\varepsilon_{xz}^\pm - \tau^{s\pm}(x)\frac{\partial w}{\partial x} \right] n_y \equiv \sigma_{xz}^{s\pm} n_y, \\ \sigma_{fx}^{s\pm} &= \left[ 2\mu^{s\pm}(x)\varepsilon_{zx}^\pm - \tau^{s\pm}(x)\frac{\partial u_x}{\partial z} \right] n_y \equiv \sigma_{zx}^{s\pm} n_y, \\ \sigma_{nx}^{s\pm} &= \tau^{s\pm}(x)u_{n,x}^s \equiv \left[ \tau^{s\pm}(x)\frac{\partial w}{\partial x} \right] n_z \end{aligned} \quad (19)$$

where  $n_y$  and  $n_z$  are the  $y$ - and  $z$ - components of the unit outward normal vector  $\mathbf{n}$  to the beam lateral surface, respectively, i.e., with  $\theta$  is the angle between the  $y$ -axis and the normal vector  $\mathbf{n}$ , then  $n_y = \cos\theta$  and  $n_z = \sin\theta$ . The subscript “ $f$ ” represents the direction of the unit tangent vector  $\mathbf{s}$  on the beam boundary.

It is essential to emphasize the fact that the in-plane shear stress tensor defined by Eq. (19) is not symmetric, and thus the values of  $\sigma_{xz}^s$  and  $\sigma_{zx}^s$  are different [98, 99]. Many authors have employed the GM-SET claiming symmetric in-plane shear stress tensor in their variational models.

## 2.2 Variational formulation

Employing the generalized elasticity theory in combination with GM-SET and MCST, the total strain energy ( $\mathbb{U}$ ) of isotropic elastic 2DFGPM deformed nanobeam can be written as follows [49, 63]:

$$\mathbb{U} = \frac{1}{2} \int_0^L \left[ \int_A \left[ \sigma_{ij}^B \varepsilon_{ij} + m_{ij} \chi_{ij} \right] dA + \oint_{\Gamma} \left[ \sigma_{ij}^s \varepsilon_{ij} \right] dS \right] dx \quad (20)$$

where  $A$  and  $\Gamma$  are, respectively, the cross-sectional area and the boundary of the beam. Substitution of Eqs. (17–19) into Eq. (18) yields

$$\begin{aligned} \mathbb{U} &= \frac{1}{2} \int_0^L \left\{ \int_A \left( \sigma_{xx}^B \varepsilon_{xx} + 2\sigma_{xz}^B \varepsilon_{xz} + 2m_{xy} \chi_{xy} + 2m_{yz} \chi_{yz} \right) dA \right. \\ &\quad \left. + \oint_{\Gamma} \left( \sigma_{xx}^s \varepsilon_{xx} + \sigma_{xf}^s \varepsilon_{xf} + \sigma_{fx}^s \varepsilon_{fx} + 2\sigma_{nx}^s \varepsilon_{nx} \right) dS \right\} dx \end{aligned} \quad (21)$$

with

$$\varepsilon_{fx} = \varepsilon_{xf} = \frac{1}{2} \left( \frac{\partial u_z}{\partial x} + \frac{\partial u_x}{\partial z} \right) n_y \equiv \frac{1}{2} \left( -\frac{\partial R(z_n)}{\partial z_n} \phi \right) n_y \equiv \varepsilon_{zx} n_y, \quad \varepsilon_{nx} = \varepsilon_{xn} = \frac{1}{2} \left( \frac{\partial u_z}{\partial x} \right) n_z = \frac{1}{2} \left( \frac{\partial w}{\partial x} \right) n_z \quad (22)$$

In light of Eqs. (17–19, 21), the total strain energy in Eq. (21) can be obtained in terms of the displacement components as

$$\begin{aligned} \mathbb{U} &= \frac{1}{2} \int_0^L \left\{ \left[ A_{xx}(x) \left( \frac{\partial u}{\partial x} \right)^2 - 2B_{xx}(x) \frac{\partial u}{\partial x} \frac{\partial^2 w}{\partial x^2} + [D_{xx}(x) + A_{xz}(x)] \left( \frac{\partial^2 w}{\partial x^2} \right)^2 + 2E_{xx}(x) \frac{\partial u}{\partial x} \frac{\partial \phi}{\partial x} \right. \right. \\ &\quad \left. \left. - 2 \left[ F_{xx}(x) + \frac{1}{2} D_{xz}(x) \right] \frac{\partial^2 w}{\partial x^2} \frac{\partial \phi}{\partial x} + \left[ H_{xx}(x) + \frac{1}{4} B_{xz}(x) \right] \left( \frac{\partial \phi}{\partial x} \right)^2 + \left[ B_{xz}(x) + \frac{1}{4} E_{xz}(x) \right] \phi^2 \right. \right. \\ &\quad \left. \left. + \left[ C_0^s \frac{\partial u}{\partial x} - C_1^s \frac{\partial^2 w}{\partial x^2} + C_2^s \frac{\partial \phi}{\partial x} \right] + C_n^s \left( \frac{\partial w}{\partial x} \right)^2 \right\} dx \end{aligned} \quad (23)$$

in which,

$$\begin{aligned} &\{ A_{xx}(x) \quad B_{xx}(x) \quad D_{xx}(x) \quad E_{xx}(x) \quad F_{xx}(x) \quad H_{xx}(x) \} \\ &\equiv \{ A_{xx}^B(x) + A_{xx}^s(x) \quad B_{xx}^B(x) + B_{xx}^s(x) \quad D_{xx}^B(x) + D_{xx}^s(x) \quad E_{xx}^B(x) + E_{xx}^s(x) \quad F_{xx}^B(x) + F_{xx}^s(x) \quad H_{xx}^B(x) + H_{xx}^s(x) \} \end{aligned} \quad (24a)$$

$$\mathcal{B}_{xz}(x) = B_{xz}^B(x) + B_m^s(x) - \frac{1}{2}B_t^s(x) \quad (24b)$$

with

$$\{A_{xx}^B(x) B_{xx}^B(x) D_{xx}^B(x) E_{xx}^B(x) F_{xx}^B(x) H_{xx}^B(x)\} = \int_{-\frac{b}{2}}^{\frac{b}{2}} \int_{-\frac{h}{2}}^{\frac{h}{2}} \mathbb{E}^B(x, z) \{1 z_n z_n^2 R(z_n) z_n R(z_n) R^2(z_n)\} dz dy \quad (25a)$$

$$B_{xz}^B(x) = \int_{-\frac{b}{2}}^{\frac{b}{2}} \int_{-\frac{h}{2}}^{\frac{h}{2}} \mu^B(x, z) \left( \frac{\partial R(z_n)}{\partial z_n} \right)^2 dz dy \quad (25b)$$

$$\{A_{xz}(x) B_{xz}(x) D_{xz}(x) E_{xz}(x)\} = \int_{-\frac{b}{2}}^{\frac{b}{2}} \int_{-\frac{h}{2}}^{\frac{h}{2}} \left[ l^2(x, z) \mu^B(x, z) \right] \left\{ 1 \left( \frac{\partial R(z_n)}{\partial z_n} \right)^2 \frac{\partial R(z_n)}{\partial z_n} \left( \frac{\partial^2 R(z_n)}{\partial z_n^2} \right)^2 \right\} dz dy \quad (25c)$$

$$\{A_{xx}^s(x) B_{xx}^s(x) D_{xx}^s(x) E_{xx}^s(x) F_{xx}^s(x) H_{xx}^s(x)\} = \oint_{\Gamma} \mathbb{E}^s(x, z) \{1 z_n z_n^2 R(z_n) z_n R(z_n) R^2(z_n)\} dS \quad (25d)$$

$$\{C_0^s(x) C_1^s(x) C_2^s(x) C_n^s(x)\} = \oint_{\Gamma} \tau^s(x, z) \{ \tau^s(x, z) z_n \tau^s(x, z) R(z_n) \tau^s(x, z) n_z^2 \tau^s(x, z) \} dS \quad (25e)$$

$$\{B_t^s(x) B_m^s(x)\} = \oint_{\Gamma} \left( \frac{\partial R(z_n)}{\partial z_n} \right)^2 n_y^2 \{ \tau^s(x, z) \mu^s(x, z) \} dS \quad (25f)$$

Accounting for the surface mass density, the kinetic energy of the 2DFGM nanobeams can be expressed as

$$\mathbb{T} = \frac{1}{2} \int_0^L \int_A \rho^B(x, z) \left[ \left( \frac{\partial u_x}{\partial t} \right)^2 + \left( \frac{\partial u_z}{\partial t} \right)^2 \right] dA dx + \frac{1}{2} \int_0^L \oint_{\Gamma} \rho^s(x, z) \left[ \left( \frac{\partial u_x}{\partial t} \right)^2 + \left( \frac{\partial u_z}{\partial t} \right)^2 \right] dS dx \quad (26)$$

Performing the integration by parts yields

$$\mathbb{T} = \frac{1}{2} \int_0^L \left[ \left( I_A(x) \frac{\partial u}{\partial t} - I_B(x) \frac{\partial^2 w}{\partial x \partial t} + I_E(x) \frac{\partial \phi}{\partial t} \right) \frac{\partial u}{\partial t} + I_A(x) \left( \frac{\partial w}{\partial t} \right) \frac{\partial w}{\partial t} - \left( I_B(x) \frac{\partial u}{\partial t} - I_D(x) \frac{\partial^2 w}{\partial x \partial t} + I_F(x) \frac{\partial \phi}{\partial t} \right) \frac{\partial^2 w}{\partial x \partial t} + \left( I_E(x) \frac{\partial u}{\partial t} - I_F(x) \frac{\partial^2 w}{\partial x \partial t} + I_H(x) \frac{\partial \phi}{\partial t} \right) \frac{\partial \phi}{\partial t} \right] dx \quad (27)$$

in which the mass moments of inertia are

$$\{I_A(x) I_B(x) I_D(x) I_E(x) I_F(x) I_H(x)\} = \int_{-\frac{b}{2}}^{\frac{b}{2}} \int_{-\frac{h}{2}}^{\frac{h}{2}} \rho^B(x, z) \{1 z_n z_n^2 R(z_n) z_n R(z_n) R^2(z_n)\} dz dy + \oint_{\Gamma} \rho^s(x, z) \{1 z_n z_n^2 R(z_n) z_n R(z_n) R^2(z_n)\} dS \quad (28)$$

A general form for the virtual work done by the forces applied on the current beam in the context of the MCST and GT-SET can be expressed as [63, 96]

$$\delta \mathbb{W} = \int_{\Omega} (\mathbf{f} \cdot \delta \mathbf{u} + \mathbf{f}_c \cdot \delta \boldsymbol{\theta}) d\Omega + \oint_{\Gamma} (\bar{\mathbf{t}} \cdot \delta \mathbf{u} + \bar{\mathbf{s}} \cdot \delta \boldsymbol{\theta}) dS \quad (29)$$

where  $\mathbf{f}$  and  $\mathbf{f}_c$  are, respectively, the resultant per unit volume of the body force and body couple and  $\bar{\mathbf{t}}$  and  $\bar{\mathbf{s}}$  represent the resultant per unit area of traction and the surface couple, respectively. When the body couple and surface couple are ignored, no compressive force is applied, and assuming that the externally applied harmonic load  $P(x, t)$  moves with a variable velocity ignoring its inertial effect, and employing zero initial conditions, we can obtain the virtual work as

$$\delta \mathbb{W} = \int_0^L \{ f_u \delta u + P(x, t) \delta w(x_Q(t)) + q \delta w \} dx + \left\{ \bar{N} \delta u + \bar{V} \delta w - (\bar{M}_c + \bar{M}_{nc}) \frac{\partial \delta w}{\partial x} - \bar{M}_c \delta \phi \right\}_0^L \quad (30)$$

where  $\overline{f}_u$  and  $\overline{q}$  denote the components of the distributed load in  $x$ - and  $z$ -directions, respectively. At the beam ends,  $\overline{N}$  and  $\overline{V}$  are the applied axial and lateral forces, respectively,  $\overline{M}_c$  and  $\overline{M}_{nc}$  are, respectively, classical and non-classical external bending moments.

The applied external moving concentrated harmonic load is given as

$$P(x, t) = P_0 \sin(\Omega_f t) \delta(x - x_Q(t)) \quad (31)$$

where  $\delta(\cdot)$  denotes the Dirac-delta function,  $P_0$  and  $\Omega$  are respectively the amplitude and frequency of the applied load. The function describing the location of the load measured from the left end of the beam ( $x = 0$ ) is defined as

$$x_Q(t) = x_0 + vt + 0.5at^2, \quad 0 \leq x_Q \leq L \quad (32)$$

where  $x_0$ ,  $v$ , and  $a$  are the initial position, initial velocity, and the constant acceleration, respectively, of the moving load, i.e.,

$$a = \begin{cases} \frac{v^2}{2L}, & t_f = 2L/v \text{ for accelerated motion} \\ 0, & t_f = L/v \text{ for uniform motion} \\ -\frac{v^2}{2L}, & t_f = 2L/v \text{ for decelerated motion} \end{cases}, \quad 0 \leq t \leq t_f \quad (33)$$

Finally, the total energy of the 2DFGPM nanobeam is given as

$$\mathbb{L} = \mathbb{T} - (\mathbb{U} + \mathbb{W}) \quad (34)$$

### 3 Solution procedure

In this section, Lagrange's equation is employed to get the system of equations of motion. For this purpose, the trigonometric Ritz method (TRM) is applied first by approximating the displacement functions  $(x, t)$   $u(x, t)$ , and  $\phi(x, t)$  by a series of trigonometric functions that satisfy the geometric boundary conditions of simply-supported 2DFGPM nanobeams as:

$$\{w(x, t) \ u(x, t) \ \phi(x, t)\} = \left\{ \sum_{r=1}^M A_r(t) \theta_{wr}(x) \ \sum_{r=1}^M B_r(t) \theta_{ur}(x) \ \sum_{r=1}^M C_r(t) \theta_{\phi r}(x) \right\} \quad (35)$$

where  $A_r$ ,  $B_r$ , and  $C_r$  are the unknown time-dependent coefficients. The admissible trigonometric functions are

$$\{\theta_{wr}(x) \ \theta_{ur}(x) \ \theta_{\phi r}(x)\} = \left\{ \sin\left(\frac{r\pi x}{L}\right) \ \frac{d\theta_{wr}(x)}{dx} \ \frac{d\theta_{wr}(x)}{dx} \right\} \quad (36)$$

Substitution of Eqs. (23, 27, 30) into Eq. (34), and then using the Lagrange's equations given by Eq. (37)

$$\frac{d}{dt} \left( \frac{\partial \mathbb{L}}{\partial \dot{q}_k} \right) - \frac{\partial \mathbb{L}}{\partial q_k} = 0, \quad k = 1, 2, 3, \dots, 3M \quad (37)$$

yields the following system of equilibrium equations:

$$[\mathbb{K}]\{q_k(t)\} + [\mathbb{M}]\{\ddot{q}_k(t)\} = \{F^t\} - \{F^{SE}\} \quad (38)$$

in which,

$$q_k = \begin{cases} A_k(t), & k = 1, 2, \dots, M \\ B_k(t), & k = M + 1, \dots, 2M \\ C_k(t), & k = 2M + 1, \dots, 3M \end{cases} \quad (39)$$

The stiffness  $[\mathbb{K}]$  and mass  $[\mathbb{M}]$  matrices in Eq. (38) are given by

$$\begin{bmatrix} \mathbb{K}_{11}(r, k) & \mathbb{K}_{12}(r, k) & \mathbb{K}_{13}(r, k) \\ \mathbb{K}_{21}(r, k) & \mathbb{K}_{22}(r, k) & \mathbb{K}_{23}(r, k) \\ \mathbb{K}_{31}(r, k) & \mathbb{K}_{32}(r, k) & \mathbb{K}_{33}(r, k) \end{bmatrix} = \int_0^L \begin{bmatrix} \overline{D}_{xx} \theta'_{wr} \theta''_{wk} + C_n^s \theta'_{wr} \theta'_{wk} & -\overline{B}_{xx} \theta'_{ur} \theta'_{wk} & -\overline{F}_{xx} \theta'_{\phi r} \theta'_{wk} \\ -\overline{B}_{xx} \theta''_{wr} \theta'_{uk} & A_{xx} \theta'_{ur} \theta'_{uk} & E_{xx} \theta'_{\phi r} \theta'_{uk} \\ -\overline{F}_{xx} \theta''_{wr} \theta'_{\phi k} & E_{xx} \theta'_{ur} \theta'_{\phi k} & \overline{H}_{xx} \theta'_{\phi r} \theta'_{\phi k} + \overline{B}_{xz} \theta_{\phi r} \theta_{\phi k} \end{bmatrix} dx \quad (40a)$$



$$\{\bar{D}_{xx} \bar{F}_{xx} \bar{H}_{xx} \bar{B}_{xz}\} = \{D_{xx} + A_{xz} F_{xx} + \frac{1}{2} D_{xz} H_{xx} + \frac{1}{4} B_{xz} B_{xz} + \frac{1}{4} E_{xz}\} \quad (40b)$$

$$\begin{bmatrix} \mathbb{M}_{11}(r, k) & \mathbb{M}_{12}(r, k) & \mathbb{M}_{13}(r, k) \\ \mathbb{M}_{21}(r, k) & \mathbb{M}_{22}(r, k) & \mathbb{M}_{23}(r, k) \\ \mathbb{M}_{31}(r, k) & \mathbb{M}_{32}(r, k) & \mathbb{M}_{33}(r, k) \end{bmatrix} = \int_0^L \begin{bmatrix} I_A \theta_{wr} \theta_{wk} + I_D \theta'_{wr} \theta'_{wk} & -I_B \theta_{ur} \theta'_{wk} & -I_F \theta_{\phi r} \theta'_{wk} \\ -I_B \theta'_{wr} \theta_{uk} & I_A \theta_{ur} \theta_{uk} & I_E \theta_{\phi r} \theta_{uk} \\ -I_F \theta'_{wr} \theta_{\phi k} & I_E \theta_{ur} \theta_{\phi k} & I_H \theta_{\phi r} \theta_{\phi k} \end{bmatrix} dx \quad (41)$$

In Eq. (38), the force vectors  $\{F^t\}$  and  $\{F^{SE}\}$  represent, respectively, the external moving load and the self-excitation due to surface energy effect,

$$\{F^t\} = \{[P_0 \sin(\Omega_f t) \theta_{wr}(x_Q)]_{k \times 1} [0]_{k \times 1} [0]_{k \times 1}\}^T, \quad k = 1, 2, \dots, M \quad (42)$$

$$\{F^{SE}\} = 0.5 \int_0^L \{-C_1^s \theta''_{wr} C_0^s \theta'_{ur} C_2^s \theta'_{\phi r}\}^T dx \quad (43)$$

To this end, the implicit time integration Newmark method, [100, 101], is utilized to solve the equations in Eq. (38). After obtaining the time-dependent coefficients  $\{A_r(t), B_r(t), C_r(t)\}$ , the displacement, velocity, and acceleration of the beam are determined at any time  $t$ ,  $0 < t < t_f$  with  $t_f = L/v$  for uniform motion and  $t_f = 2L/v$  for accelerating and decelerating motions.

In the present analysis, the following non-dimensional quantities are used:

$$\bar{w}(x, t) = \frac{w(x, t)}{D_0}, \quad D_0 = \frac{P_0 L^3}{48 E_m I}, \quad \bar{\omega}_1 = \omega_1 L^2 \sqrt{\frac{\rho_c b h}{E_c I}}, \quad \bar{v} = \frac{v}{V_c}, \quad V_c = \frac{L \omega_1}{\pi}, \quad \tau = \frac{t}{t_f} \quad (44)$$

where  $\bar{w}(x, t)$  and  $D_0$  are the normalized dynamic deflection and the static deflection of a pure metal beam under a mid-span constant load  $P_0$ , respectively.  $\omega_1$  is the non-dimensional fundamental frequency of free vibration,  $\bar{v}$  is the normalized velocity.  $V_c$  denotes the critical velocity, at which the peaks of the maximum deflections occur.  $\tau$  is the non-dimensional time ( $0 \leq \tau \leq 1$ ), i.e., the load moves away from the beam when  $\tau > 1$ , leading to a free vibration response. Additionally, for the Newmark procedure, 2000-time increments are adopted in all the forthcoming dynamic analyses.

#### 4 Model validation

This section is devoted to verifying the accuracy and convergence of the present model and solution procedure by comparing the current results with some previous works. Four different examples are presented for a simply-supported (SS) beam. Firstly and based on the classical analysis, Fig. 2 compares the present dimensionless central dynamic deflection of a SS homogeneous beam with Abu-Hilal et al. [102] for accelerated  $a > 0$ , decelerated  $a < 0$ , and uniform  $a = 0$  types of motion of the applied load at  $\bar{v} = 1$  and  $\Omega_f = 0.99875 \omega_1$ . Secondly, the peak values of the maximum normalized deflections ( $\bar{w}_p$ ) and the corresponding absolute velocities ( $v_p$ ) of a SS TFGM beam are predicted and compared with [70, 78] based on Euler–Bernoulli (EBT) and Timoshenko beam theories (TBT), respectively. The beam is composed of a mixture of SUS304 steel (metal) and  $\text{Al}_2\text{O}_3$  (ceramic) with the following properties:  $E_m = 210$  GPa,  $E_c = 390$  GPa,  $\rho_m^B = 7800$  kg/m<sup>3</sup>,  $\rho_c^B = 3960$  kg/m<sup>3</sup>,  $v_c = v_m = 0.3$  and  $h = 0.9$  m,  $b = 0.4$  m, and  $L = 20$  m. At an excitation frequency  $\Omega_f = 0$ , Table 1 shows that the present results agree with the published ones based on the classical formulation. Thirdly, using the PSDBT and MCST, Fig. 3 compares the predicted dimensionless frequency ( $\bar{\omega}_1$ ) of free vibration of a SS 2DFGM microbeam with [103]. The properties are taken as  $E_m = 201.04$  GPa,  $E_c = 349.55$  GPa,  $v_m = 0.3262$ ,  $v_c = 0.24$ ,  $\rho_m^B = 8166$  kg/m<sup>3</sup>, and  $\rho_c^B = 3800$  kg/m<sup>3</sup> and  $l_m = l_c = 0.25h$  and the geometrical parameters are  $h = b = 15$   $\mu$ m, and  $L = 100h$ .

Finally, consider a SS 2DFGPM SUS304/ $\text{Al}_2\text{O}_3$  microbeam having the material properties mentioned above with the gradient indices  $k_x = k_z = 0.5$ , and the MLSP  $l_m = l_c = 0.5h$ , [91]. The beam has thickness  $h = 10$   $\mu$ m, width  $b = 1$   $\mu$ m, and length  $L = 20h$ . The dimensionless central deflections are plotted in Fig. 4 at  $\bar{v} = 0.2$  for even and uneven porosity distributions. The maximum dynamical magnification factors, i.e., peak values of the maximum normalized deflections ( $\bar{w}_p$ ), and the corresponding dimensionless velocities ( $\bar{v}_p$ ) are detected and compared with [91] as tabulated in Table 2 at a porosity ratio  $\alpha = 0.1$  in the uneven case. From the comparison studies presented in Figs. 2, 3, 4 and Tables 1 and 2, the newly developed model and solution methodology can accurately predict the dynamical behavior of a moving force of SS 2DFGPM beams.

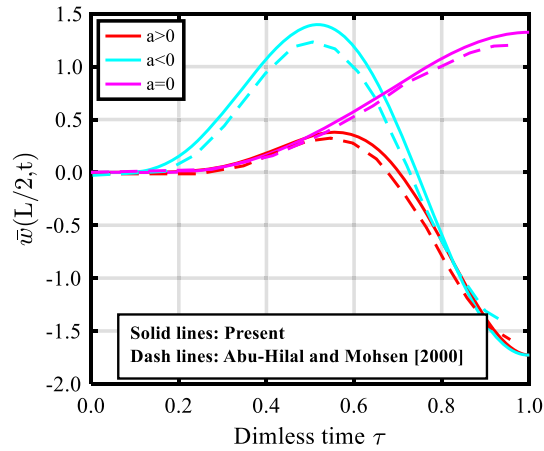


**Fig. 2** Comparison of the dimensionless central dynamic deflection of a SS homogeneous beam due to different types of motion of the applied load

**Table 1** Comparison of the peak values of maximum normalized dynamic deflection  $\bar{w}_p$  and corresponding absolute velocity  $v_p$  for a SS TFGM beam using the classical analysis

Source		$k_z = 0.2$	$k_z = 0.5$	$k_z = 1.0$	$k_z = 2.0$	Pure Al	Pure Al <sub>2</sub> O <sub>3</sub>
$\bar{w}_p$	Present (PSDBT)	1.0407	1.1510	1.2575	1.3458	1.7424	0.9384
	Nguyen et al. [78] (TBT)	1.0402	1.1505	1.2566	1.3446	1.7420	0.9380
	Simsek and Kocatürk [70] (EBT)	1.0344	1.1444	1.2503	1.3376	1.7324	0.9328
$v_p$	Present (PSDBT)	219	195	177	163	131	250
	Nguyen et al. [78] (TBT)	222	197	178	163	131	251
	Simsek and Kocatürk [70] (EBT)	222	198	179	164	132	252

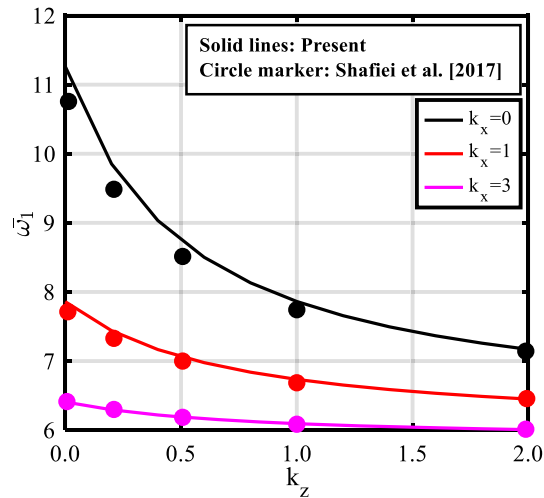


**Fig. 3** Comparison of the dimensionless fundamental frequency of a SS 2DFGM microbeam using MCST

**Table 2** Comparison of the peak values of maximum normalized dynamic deflection  $\bar{w}_p$  and corresponding dimensionless velocity  $\bar{v}_p$  for a SS 2DFGM microbeam with uneven porosity using MCST ( $k_x = k_z = 0.5$ ,  $l_m = l_c = l$ ,  $\alpha = 0.1$ )

Source		$l/h = 0$	$l/h = 0.1$	$l/h = 0.25$	$l/h = 0.5$	$l/h = 1$
$\bar{w}_p$	Present	1.3320	1.2723	1.0298	0.6128	0.2340
	Zhang and Liu [91]	1.3271	1.2658	1.0296	0.6154	0.2363
$\bar{v}_p$	Present	0.6089	0.6101	0.6126	0.6113	0.6100
	Zhang and Liu [91]	0.6050	0.6050	0.6008	0.6050	0.6092

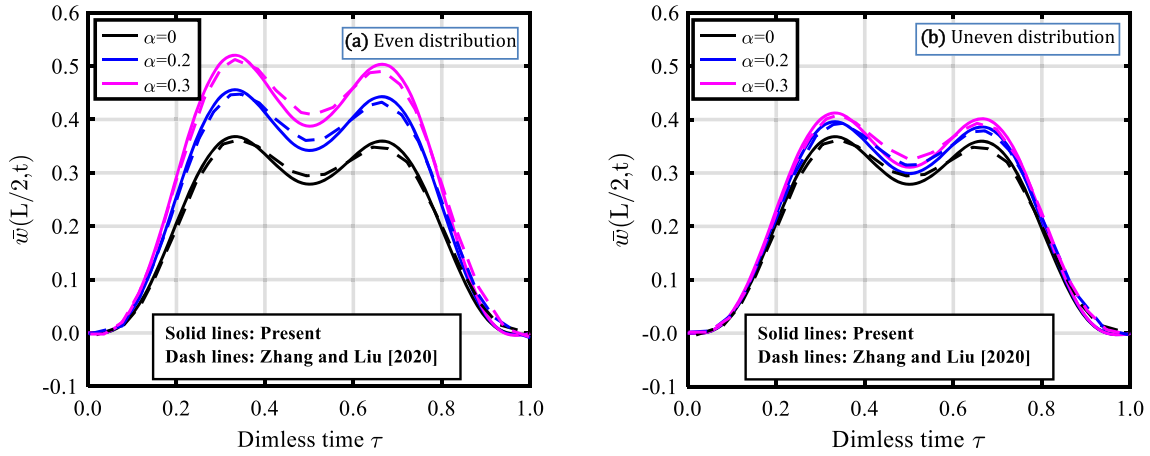


**Fig. 4** Comparison of the dimensionless central dynamic deflection of a SS 2DFGM microbeam using MCST ( $k_x = k_z = 0.5$ ,  $l_m = l_c = 0.5h$ ,  $\bar{v} = 0.2$ ) at various porosity ratios for **a** even and **b** uneven distributions

**Table 3** Material properties of bulk and surface continua of 2DFGM Al/Si nanobeam

Phase	Bulk continuum			Surface continuum		
	Young's modulus $E$ (GPa)	Poisson's ratio $\nu$	mass density $\rho^B$ (kg/m <sup>3</sup> )	Residual stress $\tau^s$ (N/m)	Elastic constants (N/m) $\mu^s$ $\lambda^s$	Mass density $\rho^s$ (kg/m <sup>2</sup> )
Aluminum (metal)	90	0.23	2700	0.5689	-5.4251    3.4939	5.461
Silicon (ceramic)	210	0.24	2331	0.6056	-2.7779    -4.4039	3.1688

## 5 Numerical results and discussion

In this section, the influences of different key parameters on the dynamical response of 2DFGM nanobeams under a moving harmonic load are extensively explored, i.e., the transverse and axial gradient indices, distribution and volume fraction ratio of porosity, velocity, frequency, and motion type of the moving force, and the small-scale due to the microstructure and surface energy. Consider a simply-supported 2DFGM nanobeam made of aluminum (Al) and silicon (Si) with the material properties in Table 3, [63, 64, 104]. Since the MLSP differs from one material to another, it is unrealistic to assume a constant MLSP in FGMs or ignore porosity's impact on its effective value.

Unfortunately, the open literature includes no available experimental data for the MLSP of FGM Al/Si, and therefore, the MLSP of silicon -to-that of aluminum ratio ( $l_c/l_m$ ) can be assumed, thus, we take  $l_m = 2h/3$  and  $l_c = 3l_m/4$  for, respectively, metal and ceramic phases [47, 65, 105]. The dimensions of the nanobeam are  $h = b = 10$  nm and  $L = 20h$ . All material and geometrical parameters are kept unchanged throughout the forthcoming results, except other values are determined. Figure 5 depicts the dependency of the distances, indicating the location of the physical neutral axis ( $e_n$  and  $r_n$ ), on the axial gradient index and porosity distribution of the 2DFGM beam.

### 5.1 Influence of the gradation indices

Figures 6 and 7 illustrate the variation of the maximum normalized central dynamic deflection (dynamic magnification factor,  $\bar{w}_{max}(L/2, t)$ ) versus the dimensionless moving velocity at different values of  $k_z$  and  $k_x$ , respectively. Both even and uneven distributions are considered at  $\alpha = 0.1$ . For a straightforward exploration of the non-classical small-scale effects, we employed the full non-classical couple stress-surface energy model

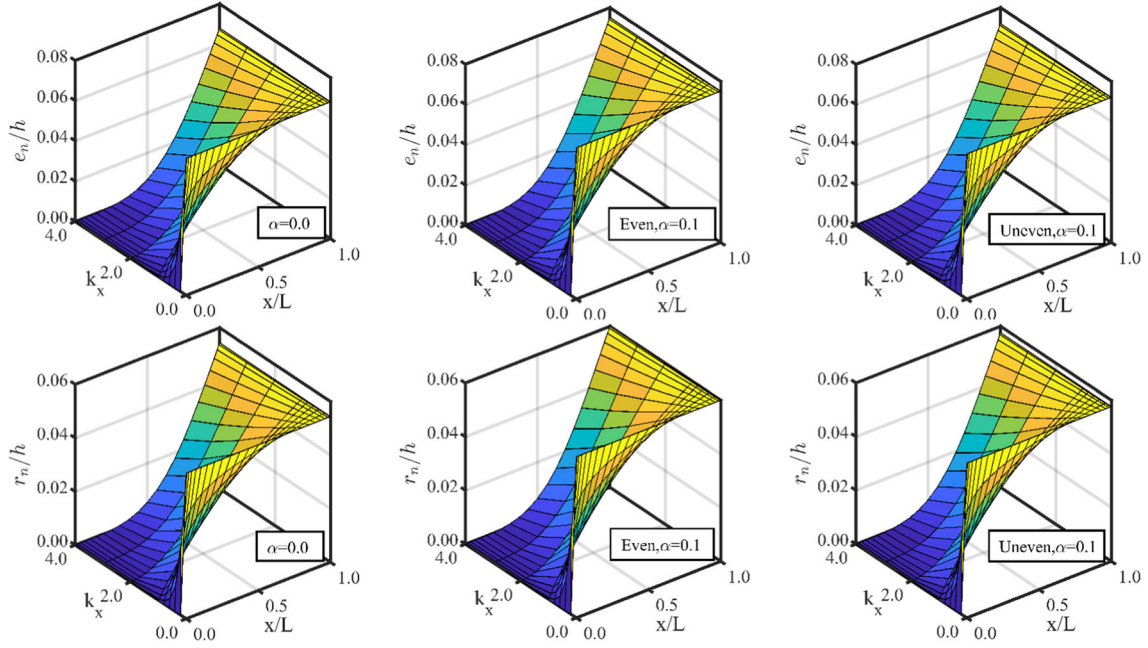


**Fig. 5** Influence of the axial gradient index on the deviations  $e_n$  and  $r_n$  along the beam length for perfect, even, and uneven cases ( $k_z = 1$ )

“CSSE” and the three special cases: classical “CL”, couple stress “CS”, and surface energy “SE” formulations in the absence of surface energy and microstructure ( $l = 0$ ,  $\tau^s = \mu^s = \lambda^s = \rho^s = 0$ ), surface energy ( $\tau^s = \mu^s = \lambda^s = \rho^s = 0$ ), and microstructure ( $l = 0$ ), respectively.

It is depicted from Figs. 6 and 7 that  $\bar{w}_{max}(L/2, t)$  in the entire time history both increases and decreases, it then increases to reach the peak value when the velocity reaches a specific value, and then after  $\bar{w}_{max}$  gradually decreases as the moving load velocity increases [106]. The velocity at which  $\bar{w}_{max}$  attains its peak value is denoted as the beam critical velocity [107]. At lower velocities of the moving load, the repeated increase, and decrease of the  $\bar{w}_{max}$  is due to the beam oscillations. For different velocities and gradient indices, incorporating the non-classical effects reduce the predicted  $\bar{w}_{max}$ . The CL formulation gives the highest  $\bar{w}_{max}$ , followed by SE, CS, and CSSE formulations, respectively, which is attributed to the stiffness-hardening effect by the couple stress and surface energy. A stiffer nanobeam can resist the moving load more than the soft one. For the same porosity ratio, a higher  $\bar{w}_{max}$  is noticed with the even distribution of porosity. Generally, the trends of the curves are independent of the gradient indices, porosity distribution, and the adopted non-classical formulations.

Table 4 provides the extracted peak dynamic magnification factors using the non-classical formulations-to-that using on the classical formulation ( $\bar{w}_p^r = \bar{w}_p^{NC} / \bar{w}_p^{CL}$ ) and their corresponding ratios of the critical velocities ( $v_p^r = v_p^{NC} / v_p^{CL}$ ). From Table 4 and Figs. 6 and 7, it can be discerned that rising  $k_z$  or  $k_x$  shows a considerable rise in the maximum normalized dynamic deflections, which is observed for the different formulations. This is because the volume fraction of metal constituent increases by increasing the gradient indices, and thus the effective rigidity of the beam decreases. Even distribution of porosity yields higher  $\bar{w}_p$  and lower  $v_p$  than those of uneven distribution. Additionally, the dynamical response is more sensitive to varying  $k_x$  than  $k_z$ . Furthermore, it is noticed that employing the non-classical formulation has a noticeable influence on the predicted response of the 2DFGPM nanobeam under investigation, as all the non-classical microstructure and surface energy parameters are spatially dependent via the gradient indices and the porosity ratio. Also, increasing the gradient indices enlarges the non-classical effects, especially for the uneven distribution. However, applying the CL formulation considerably overestimates  $\bar{w}_p$  and underestimates  $v_p$ .

Figure 8 displays the mutual effect of the thickness and length gradient indices on the maximum normalized central dynamic deflection  $\bar{w}_{max}$  due to an accelerated moving load for  $\bar{v} = 0.8, 1.2$ , and  $1.4$  and  $\alpha = 0.1$ . Under the same conditions, the predicted  $\bar{w}_{max}$  are tabulated in Table 5. Also, for the different studied moving velocities and the employed formulations,  $\bar{w}_{max}$  remarkably increases by increasing the gradient indices. The highest and lowest values of  $\bar{w}_{max}$  of the nanobeam are achieved with almost pure metal ( $k_x = k_z = 10$ ) and pure



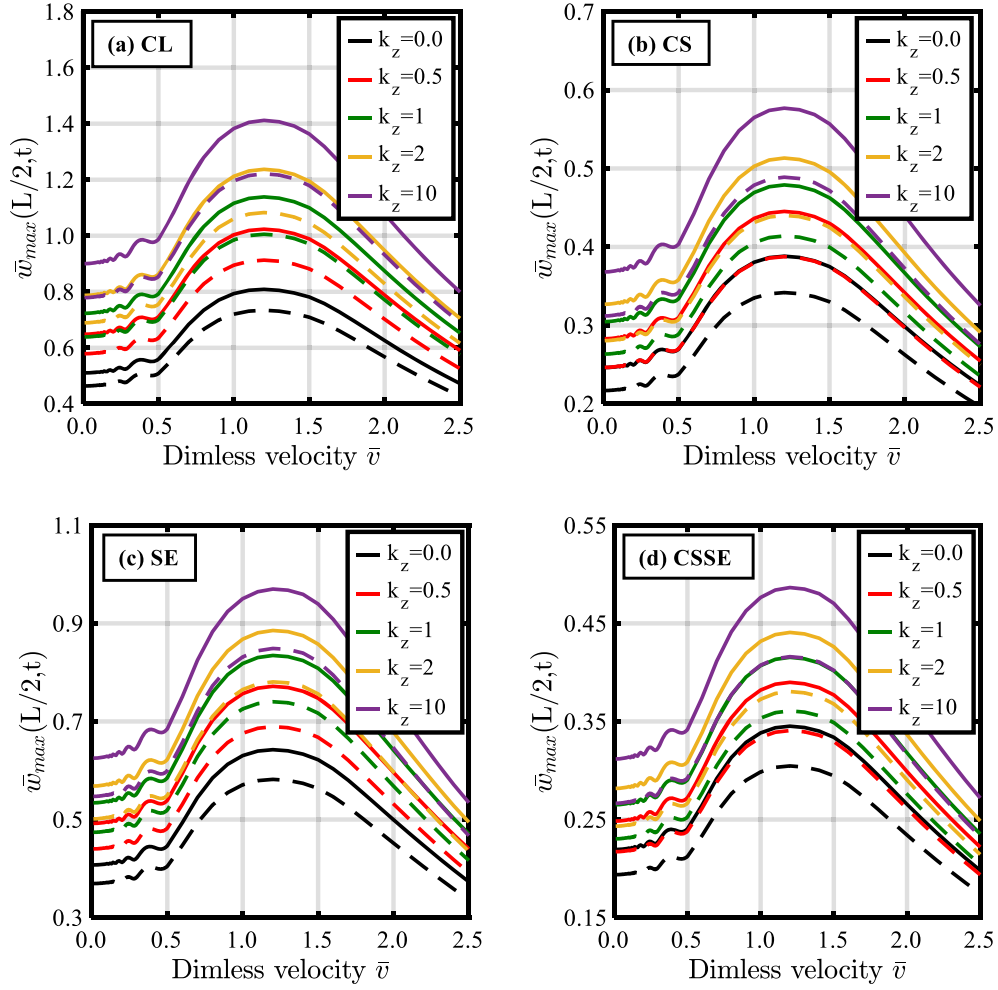


**Fig. 6** Influence of the transverse gradient index on the variation of the maximum normalized central dynamic deflection with the velocity of an accelerated moving load ( $k_x = 0.5$ ), (—) even, (- -) uneven porosity

ceramic ( $k_x = k_z = 0$ ) materials, respectively. Figures 9 and 10 show that for both CL and CSSE formulations, the gradation indices, porosity distribution, and moving velocity considerably affect the amplitude of dynamic deflection. The shapes of the time histories curves are slowly affected by the gradation indices and the porosity distribution and strongly affected by the moving velocity. The number of vibration cycles of the nanobeam is enlarged at low velocities of the moving load because the moving load velocity -to- the critical velocity ratio becomes low. According to Figs. 6, 7, 8, 9 and 10, it is extracted that the selection of the gradient indices and porosity distribution can control the dynamical response of 2DFGPM nanobeams.

## 5.2 Influence of distribution and ratio of porosity

Based on CL and CSSE analyses, Fig. 11 shows the effect of the ratio and distribution of porosity on the variation of the dimensionless maximum central deflection versus the dimensionless time at  $\bar{v} = 0.4$ ,  $\Omega_f = 0.4 \omega_1$ , and  $k_x = k_z = 1$ . According to the mathematical formulation in Eqs. (1–4), introducing the porosity effect decreases the effective properties of 2DFGPM nanobeam, and thus, its total rigidity is significantly reduced, as shown in Fig. 12, which increases the predicted dynamic deflection. Figure 12 shows the effective stiffness  $D_{xx}(x)$ , Eq. (22a), versus the length of 2DFGPM nanobeam at all the cases illustrated in Fig. 11. It is obvious that the stiffness of CSSE cases are greater than the corresponding CL cases. As a result, the predicted deflection of CSSE is less than the classical ones. Moreover, the even porosity distribution has a

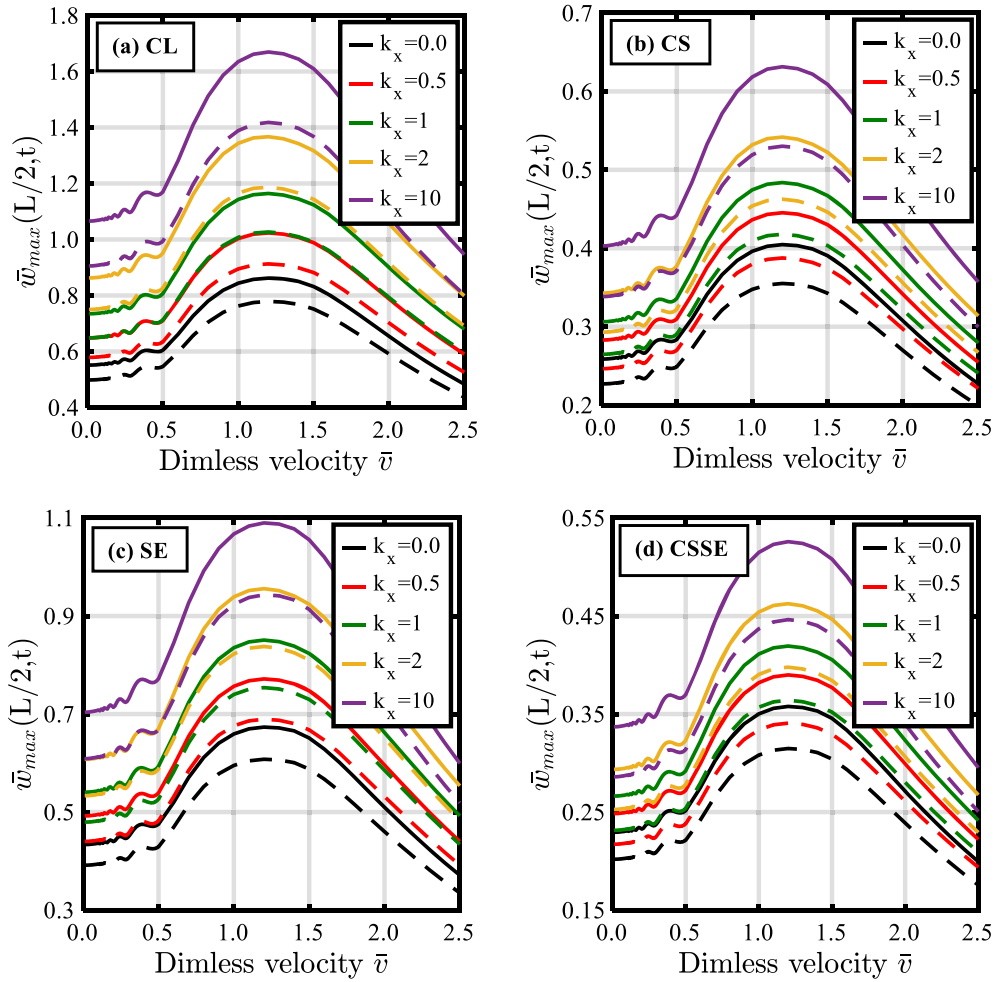


**Fig. 7** Influence of the axial gradient index on the variation of the maximum normalized central dynamic deflection with the velocity of an accelerated moving load ( $k_z = 0.5$ ), (—) even, (---) uneven porosity

more significant effect on the nanobeam stiffness. Generally speaking, porous materials are less stiff than non-porous materials due to the presence of voids (pores) within their structure. These pores reduce the effective cross-sectional area of the material, leading to lower resistance to deformation under a load. Additionally, porosity decreases the density resulting in a decrease in its inertia, which influences the predicted dynamic response. Regarding Figs. 11, 12, it is depicted that for CL and CSSE formulations, the dynamic deflection associated with the uneven distribution is much lower than that associated with the even one. Also, the porosity ratio increment significantly influences the response for the even distribution than the uneven one (see Fig. 12). Since the porosity effect is included in the evaluation of graded MLSP and surface parameters, employing the CSSE formulation enhances the porosity ratio impact on the dynamical response.

### 5.3 Influence of the moving load acceleration

Figure 13 depicts the dynamical response of a 2DFGM nanobeam with even porosity at different load motions, i.e., accelerated  $a > 0$ , uniform  $a = 0$ , and decelerated  $a < 0$ . The moving load has a frequency  $\Omega_f = \omega_1$  and a velocity  $\bar{v} = 0.1, 0.4$ . CL and CSSE formulations are considered at  $k_x = k_z = 1$  and  $\alpha = 0.1$ . It is noticeable that the load uniform motion yields the lowest maximum dynamic deflection compared with the decelerated and accelerated motions, regardless of moving velocity. Also, vibration cycles due to the accelerated motion are much lower than that of the decelerated and uniform ones, especially at the low values of dimensionless

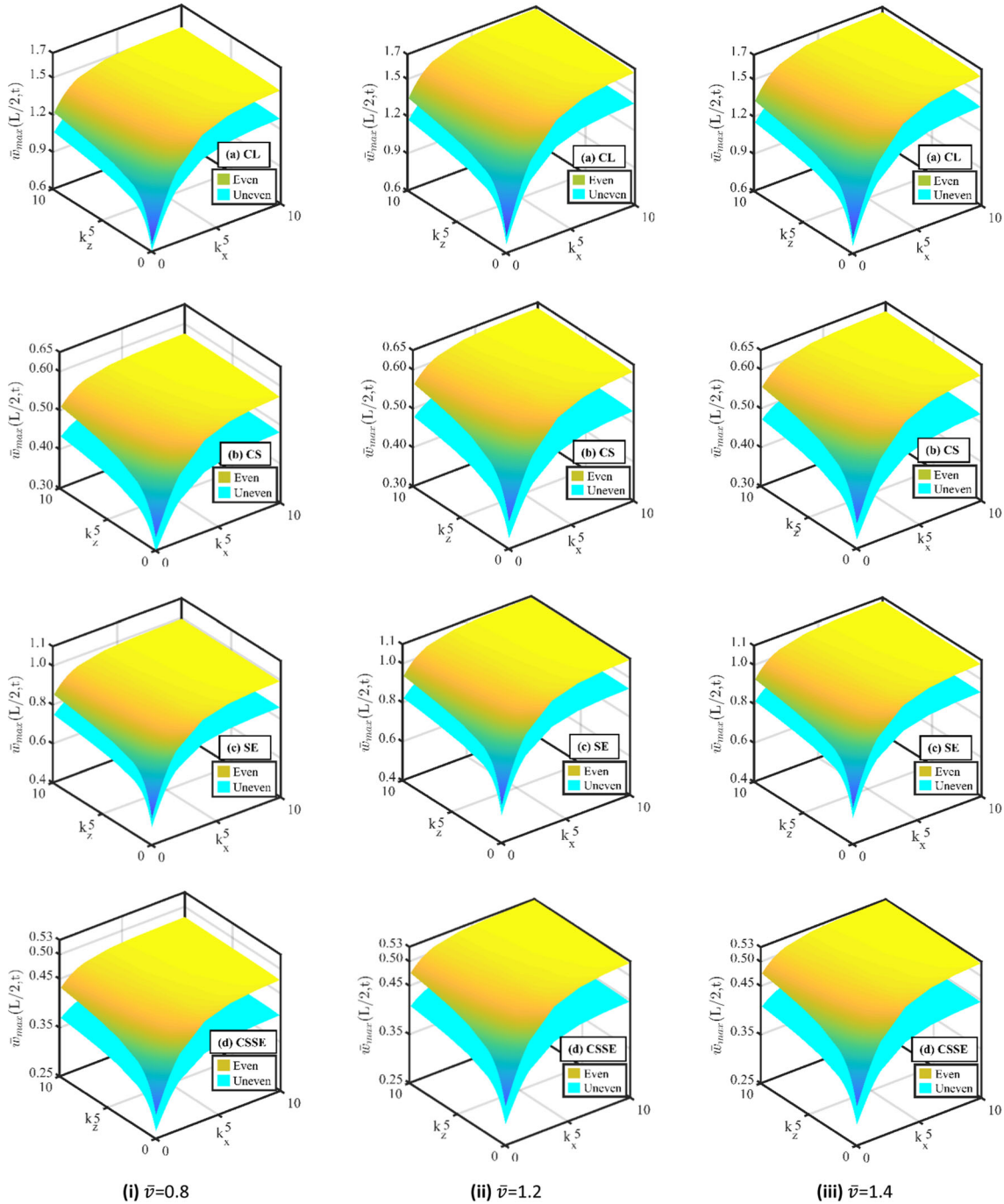


**Fig. 8** Mutual influence of the two gradient indices on the dynamic magnification factor under an accelerated moving load considering even and uneven distributions ( $\alpha = 0.1$ ) at different dimensionless moving velocities

time and moving velocity. With time progress, vibration cycles are almost identical for both accelerated and decelerated types. These differences in the dynamic response are attributed to the different kinematics of each motion type. The deflection amplitudes of accelerated and decelerated motions are identical when the dimensionless time reaches unity but still much greater than those obtained by the uniform motion. For all motion types, the vibration cycles are significantly reduced at higher moving velocities. Employing the CSSE analysis significantly decreases the dynamic deflection and does not influence vibration cycles.



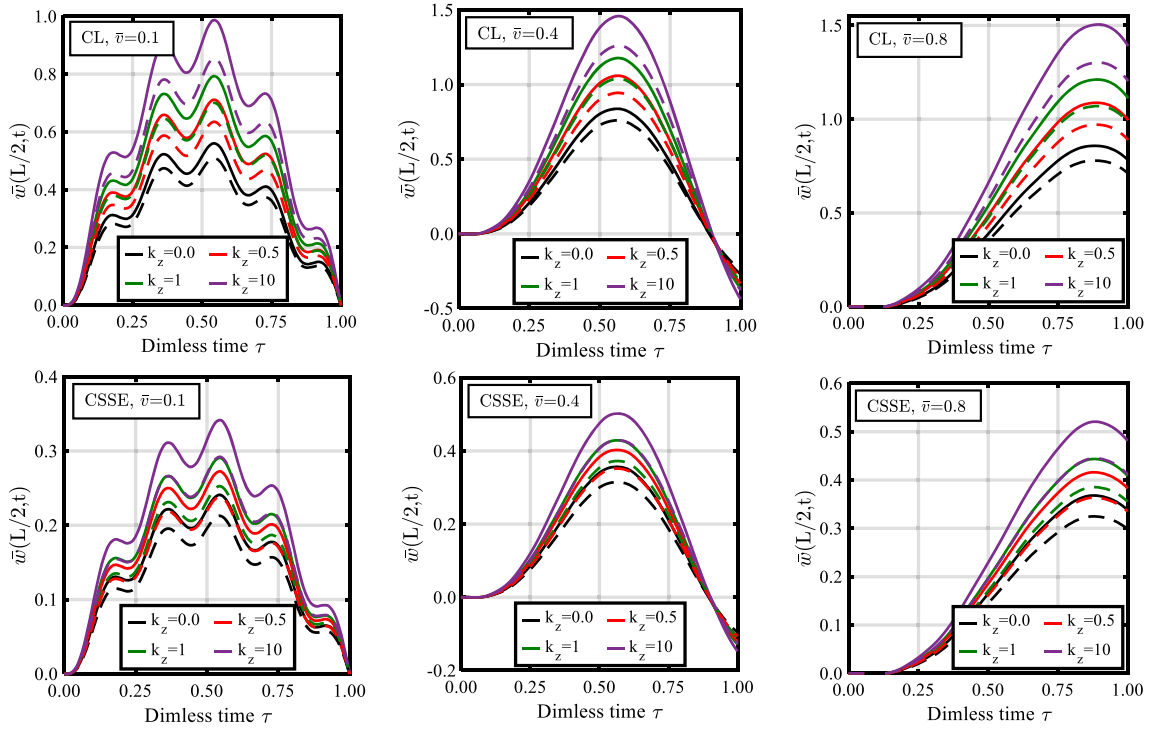


**Fig. 9** Influence of  $k_z$  on the dimensionless central deflection versus time under a uniform moving load ( $k_x = 0.5$ ,  $\alpha = 0.1$ ) at  $\bar{v} = 0.1, 0.4$ , and  $0.8$ , (—) even, (---) uneven porosity

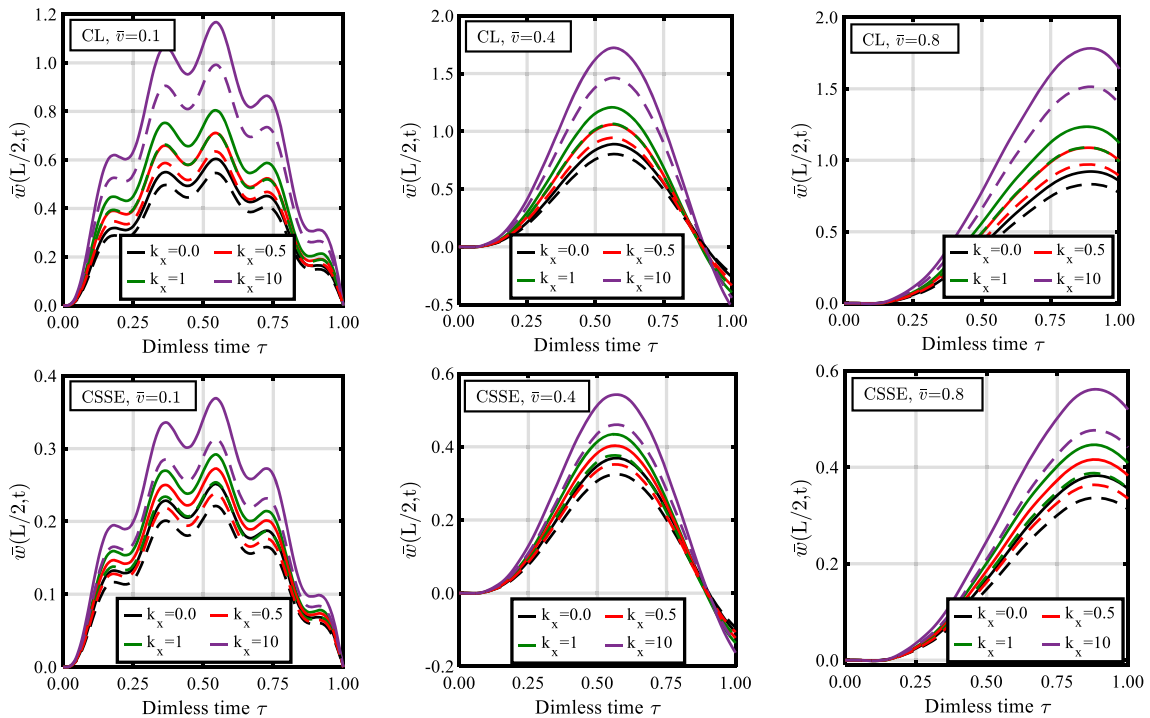


**Fig. 10** Influence of  $k_x$  on the dimensionless central deflection versus time under a uniform moving load ( $k_z = 0.5$ ,  $\alpha = 0.1$ ) at  $\bar{v} = 0.1, 0.4$ , and  $0.8$ , (—) even, (---) uneven porosity

**Table 5** Maximum dimensionless central deflection -to- the corresponding classical deflection  $\bar{w}_{max}^r(L/2, t)$  of the 2DFGPM nanobeam

$\bar{v}$	$k_z$	Porosity	CS formulation				SE formulation				CSSE formulation			
			Axial gradient index $k_x$											
			0.0	0.5	1	4	0.0	0.5	1	4	0.0	0.5	1	4
0.1	0.0	Even	0.5400	0.4824	0.4474	0.3892	0.8301	0.7981	0.7680	0.6848	0.4861	0.4299	0.3941	0.3297
		Uneven	0.5210	0.4678	0.4359	0.3835	0.8270	0.7966	0.7688	0.6942	0.4697	0.4178	0.3853	0.3277
	0.5	Even	0.4692	0.4364	0.4169	0.3842	0.7865	0.7589	0.7356	0.6766	0.4160	0.3831	0.3625	0.3242
		Uneven	0.4556	0.4257	0.4082	0.3790	0.7858	0.7602	0.7391	0.6868	0.4051	0.3752	0.3566	0.3228
	1	Even	0.4442	0.4215	0.4079	0.3831	0.7611	0.7386	0.7199	0.6726	0.3896	0.3666	0.3518	0.3225
		Uneven	0.4331	0.4124	0.4001	0.3781	0.7626	0.7420	0.7251	0.6832	0.3815	0.3605	0.3472	0.3213
	4	Even	0.4295	0.4153	0.4053	0.3832	0.7253	0.7106	0.6981	0.6667	0.3691	0.3550	0.3446	0.3212
		Uneven	0.4195	0.4066	0.3976	0.3780	0.7305	0.7171	0.7058	0.6781	0.3631	0.3501	0.3408	0.3202
0.6	0.0	Even	0.5400	0.4799	0.4437	0.3875	0.8296	0.7977	0.7674	0.6841	0.4860	0.4276	0.3909	0.3282
		Uneven	0.5211	0.4655	0.4325	0.3820	0.8265	0.7961	0.7682	0.6935	0.4696	0.4157	0.3823	0.3264
	0.5	Even	0.4692	0.4350	0.4149	0.3833	0.7859	0.7583	0.7349	0.6758	0.4159	0.3818	0.3606	0.3233
		Uneven	0.4556	0.4244	0.4064	0.3782	0.7852	0.7596	0.7384	0.6860	0.4050	0.3740	0.3550	0.3220
	1	Even	0.4442	0.4206	0.4065	0.3824	0.7604	0.7379	0.7191	0.6717	0.3895	0.3657	0.3505	0.3218
		Uneven	0.4332	0.4116	0.3989	0.3774	0.7619	0.7413	0.7243	0.6824	0.3814	0.3597	0.3461	0.3206
	4	Even	0.4295	0.4147	0.4043	0.3825	0.7244	0.7098	0.6973	0.6658	0.3690	0.3544	0.3436	0.3204
		Uneven	0.4196	0.4060	0.3967	0.3774	0.7296	0.7163	0.7050	0.6772	0.3630	0.3495	0.3399	0.3195
0.8	0.0	Even	0.5402	0.4792	0.4433	0.3877	0.8276	0.7965	0.7664	0.6820	0.4856	0.4266	0.3902	0.3279
		Uneven	0.5213	0.4649	0.4322	0.3822	0.8245	0.7948	0.7671	0.6913	0.4692	0.4148	0.3817	0.3261
	0.5	Even	0.4694	0.4347	0.4147	0.3834	0.7836	0.7565	0.7331	0.6732	0.4155	0.3811	0.3600	0.3229
		Uneven	0.4558	0.4242	0.4063	0.3784	0.7828	0.7577	0.7366	0.6834	0.4046	0.3733	0.3545	0.3217
	1	Even	0.4444	0.4204	0.4064	0.3825	0.7578	0.7357	0.7169	0.6689	0.3891	0.3651	0.3500	0.3213
		Uneven	0.4333	0.4115	0.3988	0.3776	0.7593	0.7390	0.7221	0.6796	0.3810	0.3591	0.3456	0.3203
	4	Even	0.4297	0.4147	0.4043	0.3826	0.7214	0.7070	0.6945	0.6626	0.3685	0.3537	0.3430	0.3200
		Uneven	0.4199	0.4061	0.3967	0.3776	0.7267	0.7135	0.7022	0.6740	0.3626	0.3490	0.3394	0.3191
1.4	0.0	Even	0.5402	0.4804	0.4452	0.3890	0.8271	0.7960	0.7658	0.6818	0.4853	0.4275	0.3917	0.3288
		Uneven	0.5213	0.4660	0.4340	0.3835	0.8240	0.7944	0.7665	0.6911	0.4690	0.4156	0.3831	0.3270
	0.5	Even	0.4694	0.4354	0.4159	0.3842	0.7829	0.7558	0.7325	0.6729	0.4153	0.3815	0.3609	0.3235
		Uneven	0.4559	0.4248	0.4073	0.3791	0.7821	0.7571	0.7360	0.6831	0.4044	0.3737	0.3552	0.3221
	1	Even	0.4444	0.4209	0.4072	0.3831	0.7570	0.7350	0.7162	0.6684	0.3889	0.3653	0.3505	0.3217
		Uneven	0.4334	0.4120	0.3996	0.3782	0.7585	0.7383	0.7214	0.6791	0.3808	0.3594	0.3460	0.3206
	4	Even	0.4298	0.4150	0.4048	0.3832	0.7203	0.7060	0.6936	0.6619	0.3683	0.3538	0.3433	0.3203
		Uneven	0.4199	0.4064	0.3972	0.3781	0.7256	0.7125	0.7013	0.6733	0.3624	0.3491	0.3397	0.3194
1.6	0.0	Even	0.5402	0.4791	0.4441	0.3886	0.8264	0.7960	0.7665	0.6833	0.4852	0.4263	0.3908	0.3288
		Uneven	0.5213	0.4647	0.4329	0.3830	0.8233	0.7945	0.7671	0.6924	0.4690	0.4145	0.3822	0.3269
	0.5	Even	0.4695	0.4345	0.4151	0.3838	0.7823	0.7561	0.7333	0.6740	0.4152	0.3808	0.3602	0.3233
		Uneven	0.4558	0.4240	0.4066	0.3788	0.7814	0.7572	0.7367	0.6840	0.4042	0.3730	0.3546	0.3220
	1	Even	0.4443	0.4203	0.4066	0.3828	0.7562	0.7352	0.7167	0.6692	0.3886	0.3648	0.3499	0.3215
		Uneven	0.4334	0.4113	0.3990	0.3779	0.7576	0.7384	0.7219	0.6798	0.3807	0.3588	0.3454	0.3204
	4	Even	0.4298	0.4145	0.4042	0.3829	0.7196	0.7059	0.6936	0.6622	0.3682	0.3533	0.3427	0.3200
		Uneven	0.4199	0.4060	0.3967	0.3778	0.7248	0.7124	0.7014	0.6734	0.3622	0.3485	0.3391	0.3191

#### 5.4 Influence of the moving load velocity

The maximum normalized central dynamic deflection-dimensionless moving velocity ( $\bar{w}_{max}-\bar{v}$ ) curves of a 2DFGPM nanobeam at different frequency ratios ( $r_\Omega = \Omega_f/\omega_1$ ) are illustrated in Fig. 14 at  $\alpha = 0.1$  and  $k_x = k_z = 1$ . It is noticeable that the maximum difference in the dynamical responses obtained by even and uneven porosities is at their peaks and this difference becomes insignificant as  $\bar{v}$  increases. The higher moving velocity means faster moving load, i.e., load requires lower traveling time to reach the right end of the beam, and thus, low fluctuations in the deflection are observed. Increasing  $r_\Omega$  from 0.1 to 0.4 rises the critical moving velocity, after which the fluctuations are almost eliminated. As  $r_\Omega$  increases, the peak value of  $\bar{w}_{max}$

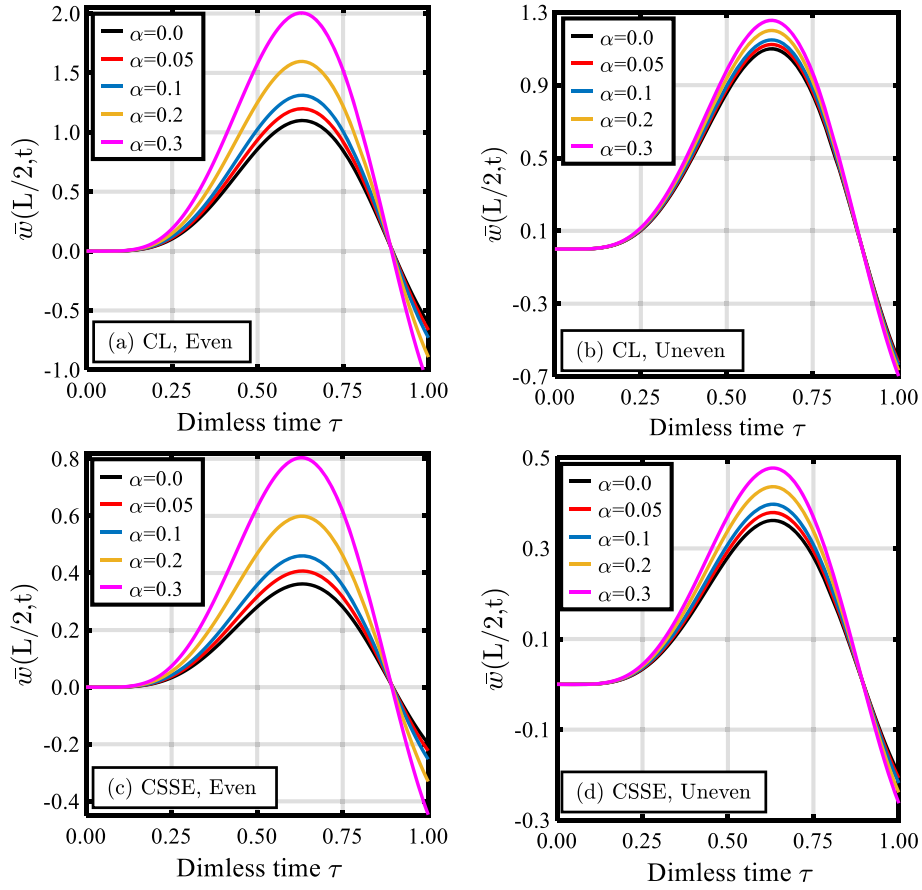


**Fig. 11** Influence of the porosity volume fraction ratio and distribution on the variation of the dimensionless central deflection versus the dimensionless time under a uniform moving load based on CL and CSSE formulations ( $k_x = k_z = 1$ )

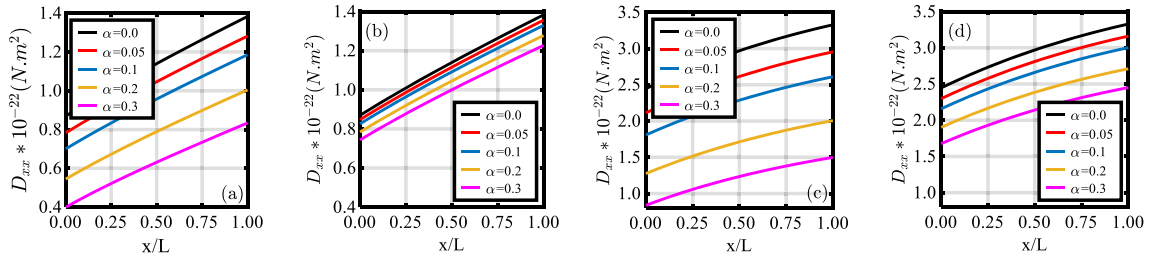


**Fig. 12** Effective stiffness  $D_{xx}(x)$  (Eq. (22a)) with respect to the length of 2DFGM nanobeam ( $k_x = k_z = 1$ ) for **a** CL-even, **b** CL-uneven, **c** CSSE-even, and **d** CSSE-uneven porosity

and its associated  $\bar{v}$  are increased. Furthermore, the inclusion of the non-classical effects via CS, SE, CSSE formulations remarkably decreases the dynamic deflection over time regardless  $\bar{v}$  and  $r_\Omega$ , whereas the overall trends of the response are almost the same. The largest and smallest dynamic deflections are obtained using CL and CSSE formulations, respectively. Additionally, for the examined 2DFGM beam, the microstructure is much more significant than that of the surface effect.

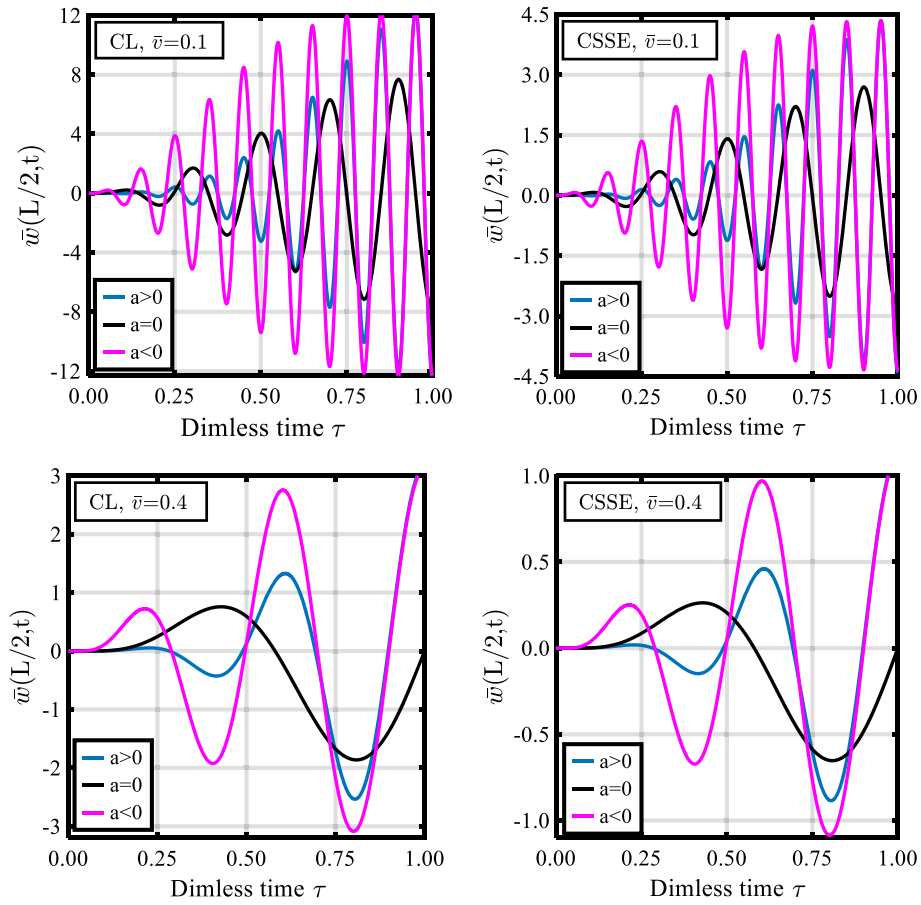


**Fig. 13** Influence of the type of applied load motion on the variation of the dimensionless central deflection versus the dimensionless time based on CL and CSSE formulations and even porosity at  $\bar{\nu} = 0.1, 0.4$  ( $\Omega_f = \omega_1, \alpha = 0.1, k_x = k_z = 1$ )

### 5.5 Influence of the moving load frequency

Figure 15 displays the maximum normalized central deflection of the 2DFGPM nanobeam versus the frequency of an accelerated moving load ( $\Omega_f$ ) at  $\bar{\nu} = 0.2$ . Various gradation indices are considered at  $\alpha = 0.1$ . By increasing  $\Omega_f$  up to a specific value that corresponds to the fundamental frequency of the nanobeam ( $\omega_1$ ), the maximum central deflection increases with small fluctuations until reaching its peak. Resonance phenomenon occurs when  $\Omega_f$  and  $\omega_1$  are the same, i.e.,  $r_\Omega = 1$ . As  $r_\Omega$  increases beyond unity, the deflection is dramatically decreased and diminishes at very high values of  $r_\Omega$ , regardless of the employed formulation and the gradient indices. Increasing the gradient indices in the transverse and/or longitudinal directions rises the metallic volume fraction, and the beam frequency decreases. Therefore, rising the gradation indices remarkably increases the peak maximum central dynamical deflection, which occurs at low frequencies. It is depicted that employing the non-classical formulations significantly decreases the maximum deflection and increases the beam frequency.

To examine the impact of  $\Omega_f$  on the deflection-time relationship of the 2DFGPM nanobeam, the normalized central deflection is plotted versus the frequency ratio and the dimensionless time ( $\bar{w}(L/2, t) - r_\Omega - \tau$ ) in Fig. 16 for  $r_\Omega \leq 0.2$  and  $r_\Omega \geq 0.2$ . Smaller  $r_\Omega$  than 0.2 results in lower amplitudes of the central deflection using both classical and non-classical analyses, Fig. 16(i). From Fig. 16 (ii) increasing  $r_\Omega$  until reaching unity, the normalized deflection approaches its highest value. Further increase in  $r_\Omega$  more than unity, i.e.,  $\Omega_f$  becomes higher than  $\omega_1$ , reduces the periodic load, and then, the deflection amplitude is considerably decreased. As  $r_\Omega$  equals about 3, the periodic load almost vanishes, and in turn, the dynamical deflection is almost eliminated.

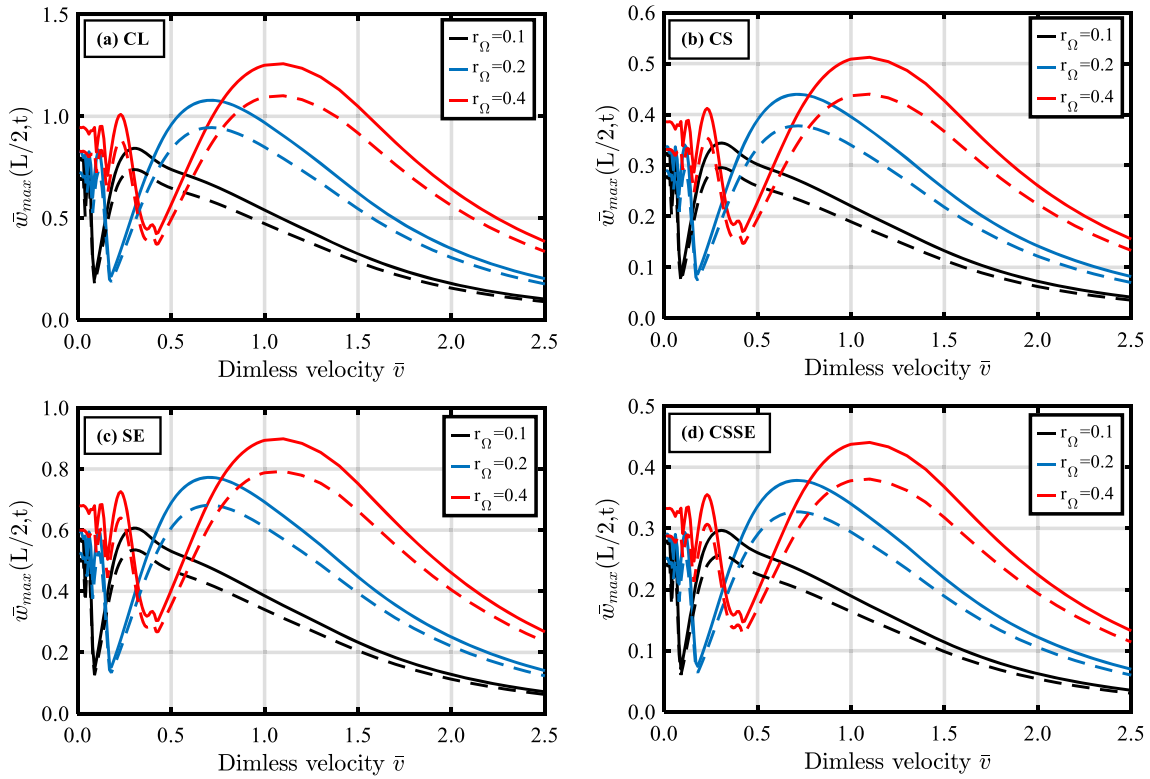


**Fig. 14** Effect of the moving load frequency on the variation of the maximum normalized central deflection versus the dimensionless moving velocity under an accelerated load ( $\alpha = 0.1$ ,  $k_x = k_z = 1$ ), (—) even, (- -) uneven porosity

## 6 Conclusions

This study investigates the dynamical response of 2DFGM nanobeams under accelerated, decelerated, and uniform harmonic loads. A new non-classical beam model is presented that incorporates the impacts of surface energy and microstructure using PSDBT, while accounting for porosity effects and 2D gradation of material parameters. The model considers the exact location of the physical neutral axis and equilibrium equations are obtained using Lagrange's equation. Numerical analysis is performed using the trigonometric Ritz method and Newmark method, with four examples solved and compared to previous studies. The study extensively investigates and analyzes the impact of various factors on the dynamical behavior of a simply-supported 2DFGM nanobeam, including power-law gradient indices, distribution and volume fraction ratio of porosity, velocity, frequency, and motion type of the load, microstructure, and surface energy. The study concludes that the presented model is valid and effective, and provides important insights into the behavior of 2DFGM nanobeams. Some important conclusions can be summarized as follows:

1. Results show that porosity reduces the overall rigidity and inertia of the nanobeam, causing an increase in dynamic deflection as the porosity ratio rises. Even porosity has a greater influence than uneven porosity, and neglecting the porosity effect leads to significant errors in predicted results.
2. Accelerated and decelerated motions of the applied load significantly influence the dynamical deflection of 2DFGM nanobeam than the uniform motion. The vibration cycles are considerably increased under an accelerated load, especially at a low moving velocity.

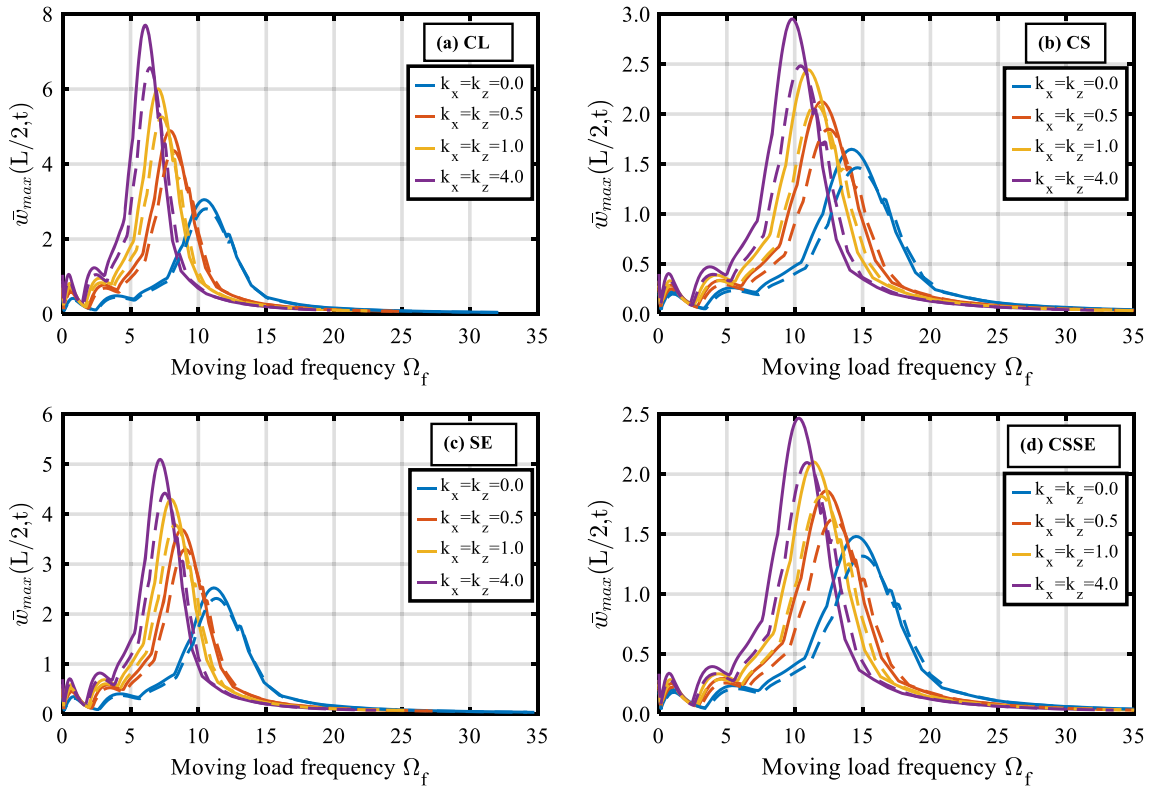


**Fig. 15** Maximum normalized central deflection versus the load frequency of an accelerated moving load at different gradation indices, ( $\alpha = 0.1$ ,  $\bar{\nu} = 0.2$ ), (—) even, (- -) uneven porosity

3. The dynamical response of 2DFGPM nanobeams is similarly affected by both transverse and axial power-law gradient indices, independent of the employed formulation and parameters of the moving load. Increasing the gradient indices leads to an increase in normalized dynamical deflection and maximum deflection while reducing the critical velocity. The effect of gradient indices is observed to increase when adopting classical analysis.
4. The dynamical deflection of the 2DFGPM nanobeam increases as the moving velocity rises to its critical value. However, beyond this critical value, the predicted deflection is significantly reduced, irrespective of the gradation indices, porosity, and formulation type. Moreover, the vibration cycles decrease considerably with an increase in moving velocity.
5. The non-classical size-dependent impact on the dynamical response is enlarged by increasing the gradient indices because the MLSP and surface parameters are spatially dependent through the same gradient indices.
6. As the frequency ratio increases, the dynamical deflection of the 2DFGPM nanobeam increases and approaches its highest value when the resonance phenomenon occurs. Also, the moving velocity affects the sensitivity of the dynamic response to the frequency.

The study highlights the importance of considering non-classical effects due to microstructure and surface energy and the potential for constructing the distribution of porosity and constituent materials to achieve desired performance under specific conditions. Importantly, ignoring the non-classical effects due to microstructure and surface energy leads to non-negligible errors in the dynamical analysis of 2DFGPM nanobeams.

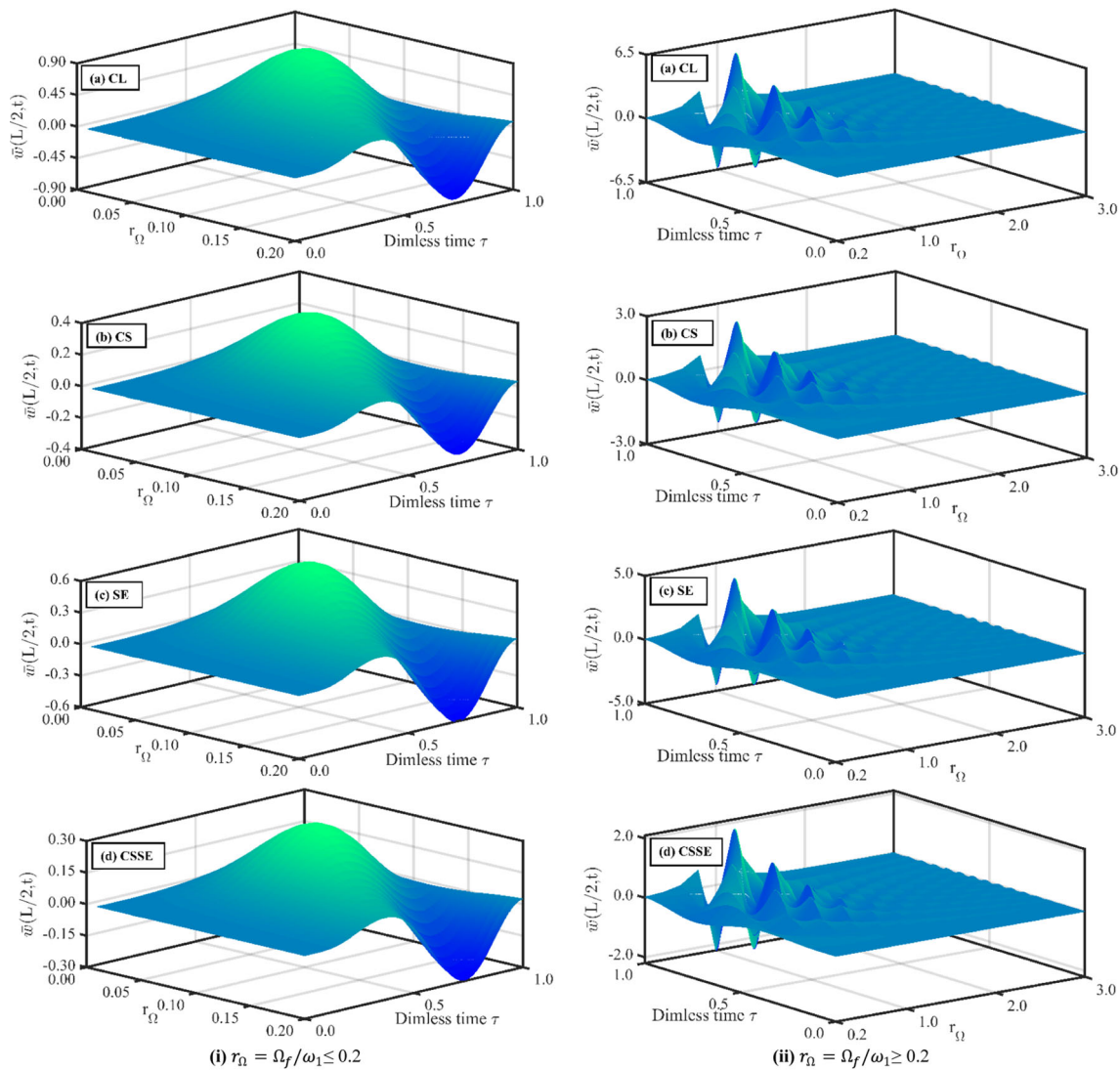


**Fig. 16** Normalized central deflection of 2DFGM nanobeam versus the frequency ratio and the dimensionless time under an accelerated moving load (even porosity,  $\alpha = 0.1$ ,  $k_x = k_z = 1$ ,  $\bar{v} = 0.2$ )

**Funding** Open access funding provided by The Science, Technology & Innovation Funding Authority (STDF) in cooperation with The Egyptian Knowledge Bank (EKB).

**Open Access** This article is licensed under a Creative Commons Attribution 4.0 International License, which permits use, sharing, adaptation, distribution and reproduction in any medium or format, as long as you give appropriate credit to the original author(s) and the source, provide a link to the Creative Commons licence, and indicate if changes were made. The images or other third party material in this article are included in the article’s Creative Commons licence, unless indicated otherwise in a credit line to the material. If material is not included in the article’s Creative Commons licence and your intended use is not permitted by statutory regulation or exceeds the permitted use, you will need to obtain permission directly from the copyright holder. To view a copy of this licence, visit <http://creativecommons.org/licenses/by/4.0/>.

**References**

1. Birman, V., Byrd, L.W.: Modeling and analysis of functionally graded materials and structures. *Appl. Mech. Rev.* **60**(5), 195–216 (2017)
2. Huang, D., Ding, H., Chen, W.: Analytical solution for functionally graded magneto-electro-elastic plane beams. *Int. J. Eng. Sci.* **45**, 467–485 (2007)
3. Thai, H.-T., Kim, S.-E.: A review of theories for the modeling and analysis of functionally graded plates and shells. *Compos. Struct.* **128**, 70–86 (2015)

4. Gupta, A., Talha, M.: Recent development in modeling and analysis of functionally graded materials and structures. *Prog. Aerosp. Sci.* **79**, 1–14 (2015)
5. Thai, H.-T., Vo, T.P., Nguyen, T.-K., Kim, S.-E.: A review of continuum mechanics models for size-dependent analysis of beams and plates. *Compos. Struct.* **177**, 196–219 (2017)
6. Tang, Y., Ma, Z.-S., Ding, Q., Wang, T.: Dynamic interaction between bi-directional functionally graded materials and magneto-electro-elastic fields: a nanostructure analysis. *Compos. Struct.* **264**, 113746 (2021)
7. Draï, A., Daikh, A., Belarbi, M., Houari, M., Aour, B., Hamdi, A., Eltaher, M.: Bending of axially functionally graded carbon nanotubes reinforced composite nanobeams. *Adv. Nano Res.* **14**(3), 211–224 (2023)
8. Ladmek, M., Belkacem, A., Daikh, A., Bessaim, A., Garg, A., Houari, M., Belarbi, M., Ouldyyerou, A.: Free vibration of functionally graded carbon nanotubes reinforced composite nanobeams. *Adv. Mater. Res.* **12**(2), 161–177 (2023)
9. Belarbi, M., Salami, S., Garg, A., Daikh, A., Houari, M., Dimitri, R., Tornabene, F.: Mechanical behavior analysis of FG-CNT-reinforced polymer composite beams via a hyperbolic shear deformation theory. *Continuum Mech. Thermodyn.* **35**, 497–520 (2023)
10. Remil, A., Belarbi, M., Bessaim, A., Houari, M., Bouamoud, A., Daikh, A., Mouffoki, A., Tounsi, A., Hamdi, A., Eltaher, M.: An Accurate Analytical Model for the Buckling Analysis of FG-CNT Reinforced Composite Beams Resting on an Elastic Foundation with Arbitrary Boundary Conditions. *Comput. Concr.* **31**(3), 267–276 (2023)
11. Daikh, A., Belarbi, M., Salami, S., Ladmek, M., Belkacem, A., Houari, M., Ahmed, H., Eltaher, M.: A three-unknown refined shear beam model for the bending of randomly oriented FG-CNT/fiber-reinforced composite laminated beams rested on a new variable elastic foundation. *Acta Mech.* (2023)
12. Fleck, N., Muller, G., Ashby, M.F., Hutchinson, J.W.: Strain gradient plasticity: theory and experiment. *Acta Metall. Mater.* **42**, 475–487 (1994)
13. Stölken, J.S., Evans, A.: A microbend test method for measuring the plasticity length scale. *Acta Mater.* **46**, 5109–5115 (1998)
14. Lam, D.C., Yang, F., Chong, A., Wang, J., Tong, P.: Experiments and theory in strain gradient elasticity. *J. Mech. Phys. Solids* **51**, 1477–1508 (2003)
15. Li, X., Bhushan, B., Takashima, K., Baek, C.-W., Kim, Y.-K.: Mechanical characterization of micro/nanoscale structures for MEMS/NEMS applications using nanoindentation techniques. *Ultramicroscopy* **97**, 481–494 (2003)
16. Liebold, C., Müller, W.H.: Comparison of gradient elasticity models for the bending of micromaterials. *Comput. Mater. Sci.* **116**, 52–61 (2016)
17. Cowley, E.R.: Lattice dynamics of silicon with empirical many-body potentials. *Phys. Rev. Lett.* **60**, 2379 (1988)
18. Admal, N.C., Tadmor, E.B.: A unified interpretation of stress in molecular systems. *J. Elast.* **100**, 63–143 (2010)
19. Farajpour, A., Ghayesh, M.H., Farokhi, H.: A review on the mechanics of nanostructures. *Int. J. Eng. Sci.* **133**, 231–263 (2018)
20. Khaniki, H.B., Ghayesh, M.H., Amabili, M.: A review on the statics and dynamics of electrically actuated nano and micro structures. *Int. J. Non-Linear Mech.* 103658 (2020).
21. Yang, F., Chong, A., Lam, D.C.C., Tong, P.: Couple stress based strain gradient theory for elasticity. *Int. J. Solids Struct.* **39**, 2731–2743 (2002)
22. Gurtin, M.E., Murdoch, A.I.: A continuum theory of elastic material surfaces. *Arch. Ration. Mech. Anal.* **57**, 291–323 (1975)
23. Gurtin, M.E., Murdoch, A.I.: Surface stress in solids. *Int. J. Solids Struct.* **14**, 431–440 (1978)
24. Barati, M.R., Shahverdi, H.: Frequency analysis of nanoporous mass sensors based on a vibrating heterogeneous nanoplate and nonlocal strain gradient theory. *Microsyst. Technol.* **24**, 1479–1494 (2018)
25. Rahmani, A., Faroughi, S., Friswell, M.: The vibration of two-dimensional imperfect functionally graded (2D-FG) porous rotating nanobeams based on general nonlocal theory. *Mech. Syst. Signal Process.* **144**, 106854 (2020)
26. Mohammadi, M., Hosseini, M., Shishesaz, M., Hadi, A., Rastgoo, A.: Primary and secondary resonance analysis of porous functionally graded nanobeam resting on a nonlinear foundation subjected to mechanical and electrical loads. *Eur. J. Mech. A/Solids* **77**, 103793 (2019)
27. Sahmani, S., Aghdam, M.M., Rabczuk, T.: Nonlinear bending of functionally graded porous micro/nano-beams reinforced with graphene platelets based upon nonlocal strain gradient theory. *Compos. Struct.* **186**, 68–78 (2018)
28. Liu, H., Liu, H., Yang, J.: Vibration of FG magneto-electro-viscoelastic porous nanobeams on visco-Pasternak foundation. *Compos. B Eng.* **155**, 244–256 (2018)
29. Aria, A.I., Rabczuk, T., Friswell, M.I.: A finite element model for the thermo-elastic analysis of functionally graded porous nanobeams. *Eur. J. Mech. A/Solids* **77**, 103767 (2019)
30. Khorasani, M., Lampani, L., Tounsi, A.: A refined vibrational analysis of the FGM porous type beams resting on the silica aerogel substrate. *Steel Compos. Struct.* **47**(5), 633–644 (2023)
31. Mesbah, A., Belabed, Z., Amara, K., Tounsi, A., Bousahla, A., Bourada, F.: Formulation and evaluation a finite element model for free vibration and buckling behaviours of functionally graded porous (FGP) beams. *Struct. Eng. Mech.* **86**(3), 291–309 (2023)
32. Bellifa, H., Selim, M., Chikh, A., Bousahla, A., Bourada, F., Tounsi, A., Benrahou, K., Al-Zahrani, M., Tounsi, A.: Influence of porosity on thermal buckling behavior of functionally graded beams. *Smart Struct. Syst.* **27**(4), 719–728 (2021)
33. Esen, I., Abdelrahman, A., Eltaher, M.: Dynamics analysis of timoshenko perforated microbeams under moving loads. *Eng. Comput.* **38**, 2413–2429 (2022)
34. Katiyar, V., Gupta, A., Tounsi, A.: Microstructural/geometric imperfection sensitivity on the vibration response of geometrically discontinuous bi-directional functionally graded plates (2D-FGPs) with partial supports by using FEM. *Steel Compos. Struct.* **45**(5), 621–640 (2022)
35. Bekkaye, T., Fahsi, B., Bousahla, A., Bourada, F., Tounsi, A., Benrahou, K., Tounsi, A., Al-Zahrani, M.: Porosity-dependent mechanical behaviors of FG plate using refined trigonometric shear deformation theory. *Comput. Concr.* **26**(5), 439–450 (2020)



36. Liu, G., Wu, S., Shahsavari, D., Karami, B., Tounsi, A.: Dynamics of imperfect inhomogeneous nanoplate with exponentially-varying properties resting on viscoelastic foundation. *Eur. J. Mech. A. Solids* **95**, 104649 (2022)
37. Van Vinh, P., Chinh, N., Tounsi, A.: Static bending and buckling analysis of bi-directional functionally graded porous plates using an improved first-order shear deformation theory and FEM. *Eur. J. Mech. A. Solids* **96**, 104743 (2022)
38. Arshid, E., Khorasani, M., Soleimani-Javid, Z., Amir, S., Tounsi, A. Porosity-dependent vibration analysis of FG microplates embedded by polymeric nanocomposite patches considering hygrothermal effect via an innovative plate theory. *Eng. Comput.* 4051–4072 (2022)
39. Cuong-Le, T., Nguyen, K., Le-Minh, H., Phan-Vu, P., Nguyen-Trong, P., Tounsi, A.: Nonlinear bending analysis of porous sigmoid FGM nanoplate via IGA and nonlocal strain gradient theory. *Adv. Nano Res.* **12**(5), 441–455 (2022)
40. Al-Osta, M., Saidi, H., Tounsi, A., Al-Dulaijan, S., Al-Zahrani, M., Sharif, A., Tounsi, A.: Influence of porosity on the hygro-thermo-mechanical bending response of an AFG ceramic-metal plates using an integral plate model. *Smart Struct. Syst.* **28**(4), 499–513 (2021)
41. Kuma, Y., Gupta, A., Tounsi, A.: Size-dependent vibration response of porous graded nanostructure with FEM and nonlocal continuum model. *Adv. Nano Res.* **11**(1), 1–17 (2021)
42. Xia, L., Wang, R., Chen, G., Asemi, K., Tounsi, A.: The finite element method for dynamics of FG porous truncated conical panels reinforced with graphene platelets based on the 3-D elasticity. *Adv. Nano Res.* **14**(4), 375–389 (2023)
43. Hadji, M., Bouhadra, A., Mamen, B., Abderahmane, M., AbdelmoumenAnis, B., Bourada, F., Bourada, M., Benrahou, K., Tounsi, A.: Combined influence of porosity and elastic foundation parameters on the bending behavior of advanced sandwich structures. *Steel Compos. Struct.* **46**(1), 1–13 (2023)
44. Nemat-All, M.: Reduction of thermal stresses by developing two-dimensional functionally graded materials. *Int. J. Solids Struct.* **40**, 7339–7356 (2003)
45. Trinh, L.C., Vo, T.P., Thai, H.-T., Nguyen, T.-K.: Size-dependent vibration of bi-directional functionally graded microbeams with arbitrary boundary conditions. *Compos. B Eng.* **134**, 225–245 (2018)
46. Karamanli, A., Vo, T.P.: Size dependent bending analysis of two directional functionally graded microbeams via a quasi-3D theory and finite element method. *Compos. B Eng.* **144**, 171–183 (2018)
47. Chen, X., Zhang, X., Lu, Y., Li, Y.: Static and dynamic analysis of the postbuckling of bi-directional functionally graded material microbeams. *Int. J. Mech. Sci.* **151**, 424–443 (2019)
48. Yu, T., Hu, H., Zhang, J., Bui, T.Q.: Isogeometric analysis of size-dependent effects for functionally graded microbeams by a non-classical quasi-3D theory. *Thin-Walled Struct.* **138**, 1–14 (2019)
49. Attia, M.A., Mohamed, S.A.: Thermal vibration characteristics of pre/post-buckled bi-directional functionally graded tapered microbeams based on modified couple stress Reddy beam theory. *Eng. Comput.* 1–27 (2020).
50. Attia, M.A., Mohamed, S.A.: Nonlinear thermal buckling and postbuckling analysis of bidirectional functionally graded tapered microbeams based on Reddy beam theory. *Eng. Comput.* 1–30 (2020).
51. Gholami, M., Vaziri, E., Moradifard, R.: Size-dependent nonlinear vibration in bi-directional functionally graded Euler–Bernoulli microbeams with an initial geometrical curvature. *J. Braz. Soc. Mech. Sci. Eng.* **43**, 1–12 (2021)
52. Nejad, M.Z., Hadi, A.: Nonlocal analysis of free vibration of bi-directional functionally graded Euler–Bernoulli nano-beams. *Int. J. Eng. Sci.* **105**, 1–11 (2016)
53. Ebrahimi-Nejad, S., Shaghghi, G.R., Miraskari, F., Kheybari, M.: Size-dependent vibration in two-directional functionally graded porous nanobeams under hygro-thermo-mechanical loading. *The European Physical Journal Plus* **134**, 465 (2019)
54. Lal, R., Dangi, C.: Thermomechanical vibration of bi-directional functionally graded nonuniform timoshenko nanobeam using nonlocal elasticity theory. *Compos. B Eng.* **172**, 724–742 (2019)
55. Ahmadi, I.: Vibration analysis of 2D-functionally graded nanobeams using the nonlocal theory and meshless method. *Eng. Anal. Boundary Elem.* **124**, 142–154 (2021)
56. Sahmani, S., Safaei, B.: Nonlocal strain gradient nonlinear resonance of bi-directional functionally graded composite micro/nano-beams under periodic soft excitation. *Thin-Walled Structures* **143**, 106226 (2019)
57. Sahmani, S., Safaei, B.: Influence of homogenization models on size-dependent nonlinear bending and postbuckling of bi-directional functionally graded micro/nano-beams. *Appl. Math. Model.* **82**, 336–358 (2020)
58. Karami, B., Janghorban, M., Rabczuk, T.: Dynamics of two-dimensional functionally graded tapered Timoshenko nanobeam in thermal environment using nonlocal strain gradient theory. *Compos. B Eng.* **182**, 107622 (2020)
59. Bessaim, A., Houari, M., Bezzina, S., Merdji, A., Daikh, A., Belarbi, M., Tounsi, A.: Nonlocal strain gradient theory for bending analysis of 2D functionally graded nanobeams. *Struct. Eng. Mech.* **86**(6), 731–738 (2023)
60. Daikh, A., Draï, A., Houari, M., Eltaher, M.: Static analysis of multilayer nonlocal strain gradient nanobeam reinforced by carbon nanotubes. *Steel Compos. Struct.* **36**(6), 643–656 (2020)
61. Abdelrahman, A., Esen, I., Daikh, A., Eltaher, M.: Dynamic analysis of FG nanobeam reinforced by carbon nanotubes and resting on elastic foundation under moving load. *Mech. Based Des. Struct. Mach.* (2021). <https://doi.org/10.1080/15397734.2021.1999263>
62. Lal, R., Dangi, C.: Dynamic analysis of bi-directional functionally graded Timoshenko nanobeam on the basis of Eringen's nonlocal theory incorporating the surface effect. *Appl. Math. Comput.* **395**, 125857 (2021)
63. Shanab, R.A., Attia, M.A.: Semi-analytical solutions for static and dynamic responses of bi-directional functionally graded nonuniform nanobeams with surface energy effect. *Eng. Comput.* **38**, 2269–2312 (2022). <https://doi.org/10.1007/s00366-020-01205-6>
64. Shanab, R.A., Attia, M.A.: On bending, buckling and free vibration analysis of 2D-FG tapered Timoshenko nanobeams based on modified couple stress and surface energy theories. *Waves Random Complex Media* **33**(3), 590–636 (2023). <https://doi.org/10.1080/17455030.2021.1884770>
65. Attia, M.A., Shanab, R.A.: Vibration characteristics of two-dimensional FGM nanobeams with couple stress and surface energy under general boundary conditions. *Aerosp. Sci. Technol.* **111**, 106552 (2021)
66. Sheng, G., Wang, X.: The geometrically nonlinear dynamic responses of simply supported beams under moving loads. *Appl. Math. Model.* **48**, 183–195 (2017)

67. Froio, D., Rizzi, E., Simões, F.M., Da Costa, A.P.: Dynamics of a beam on a bilinear elastic foundation under harmonic moving load. *Acta Mech.* **229**, 4141–4165 (2018)
68. Wang, Y., Zhu, X., Lou, Z.: Dynamic response of beams under moving loads with finite deformation. *Nonlinear Dyn.* **98**, 167–184 (2019)
69. Hosseini, M., Freidani, M., Elasto: Dynamic response analysis of a curved composite sandwich beam subjected to the loading of a moving mass. In: *Mechanics of advanced composite structures* (2020).
70. Şimşek, M., Kocatürk, T.: Free and forced vibration of a functionally graded beam subjected to a concentrated moving harmonic load. *Compos. Struct.* **90**, 465–473 (2009)
71. Gan, B.S., Kien, N.D., Ha, L.T.: Effect of intermediate elastic support on vibration of functionally graded Euler-Bernoulli beams excited by a moving point load. *J. Asian Architect. Build. Eng.* **16**, 363–369 (2017)
72. Esen, I.: Dynamic response of a functionally graded Timoshenko beam on two-parameter elastic foundations due to a variable velocity moving mass. *Int. J. Mech. Sci.* **153**, 21–35 (2019)
73. Wang, Y., Xie, K., Fu, T., Shi, C.: Vibration response of a functionally graded graphene nanoplatelet reinforced composite beam under two successive moving masses. *Compos. Struct.* **209**, 928–939 (2019)
74. Şimşek, M., Kocatürk, T., Akbaş, Ş.: Dynamic behavior of an axially functionally graded beam under action of a moving harmonic load. *Compos. Struct.* **94**, 2358–2364 (2012)
75. Wang, Y., Wu, D.: Thermal effect on the dynamic response of axially functionally graded beam subjected to a moving harmonic load. *Acta Astronaut.* **127**, 171–181 (2016)
76. Xie, K., Wang, Y., Fu, T.: Dynamic response of axially functionally graded beam with longitudinal–transverse coupling effect. *Aerosp. Sci. Technol.* **85**, 85–95 (2019)
77. Şimşek, M.: Bi-directional functionally graded materials (BDFGMs) for free and forced vibration of Timoshenko beams with various boundary conditions. *Compos. Struct.* **133**, 968–978 (2015)
78. Nguyen, D.K., Nguyen, Q.H., Tran, T.T.: Vibration of bi-dimensional functionally graded Timoshenko beams excited by a moving load. *Acta Mech.* **228**, 141–155 (2017)
79. Yang, Y., Kumpang, K., Lam, C., Lu, V.: Dynamic behaviors of tapered bi-directional functionally graded beams with various boundary conditions under action of a moving harmonic load. *Eng. Anal. Bound. Elem.* **104**, 225–239 (2019)
80. Chaikittiratana, A., Wattanasakulpong, N.: Gram-Schmidt-Ritz method for dynamic response of FG-GPLRC beams under multiple moving loads. In: *Mechanics Based Design of Structures and Machines*, pp. 1–22 (2020).
81. Nguyen, D.K., Vu, A.N.T., Le, N.A.T., Pham, V.N.: Dynamic behavior of a bidirectional functionally graded sandwich beam under nonuniform motion of a moving load. *Shock. Vib.* (2020). <https://doi.org/10.1155/2020/8854076>
82. Vu, A.N.T., Le, N.A.T., Nguyen, D.K.: Dynamic behaviour of bidirectional functionally graded sandwich beams under a moving mass with partial foundation supporting effect. *Acta Mech.* 1–23 (2021).
83. Nguyen, D.K., Tran, T.T., Pham, V.N., Le, N.A.T.: Dynamic analysis of an inclined sandwich beam with bidirectional functionally graded face sheets under a moving mass. *Eur. J. Mech. A/Solids* **88**, 104276 (2021)
84. Chen, S., Zhang, Q., Liu, H.: Dynamic response of double-FG porous beam system subjected to moving load. *Eng. Comput.* 1–20 (2021).
85. Hosseini, S., Rahmani, O.: Exact solution for axial and transverse dynamic response of functionally graded nanobeam under moving constant load based on nonlocal elasticity theory. *Meccanica* **52**, 1441–1457 (2017)
86. Ghadiri, M., Rajabpour, A., Akbarshahi, A.: Non-linear forced vibration analysis of nanobeams subjected to moving concentrated load resting on a viscoelastic foundation considering thermal and surface effects. *Appl. Math. Model.* **50**, 676–694 (2017)
87. Barati, M.R., Shahverdi, H.: Small-scale effects on the dynamic response of inhomogeneous nanobeams on elastic substrate under uniform dynamic load. *Eur. Phys. J. Plus* **132**, 1–14 (2017)
88. Babaei, A.: Forced vibration analysis of nonlocal strain gradient rod subjected to harmonic excitations. *Microsyst. Technol.* **27**, 821–831 (2021)
89. Esen, I., Daikh, A.A., Eltaher, M.A.: Dynamic response of nonlocal strain gradient FG nanobeam reinforced by carbon nanotubes under moving point load. *Eur. Phys. J. Plus* **136**, 1–22 (2021)
90. Rajasekaran, S., Khaniki, H.B.: Size-dependent forced vibration of nonuniform bi-directional functionally graded beams embedded in variable elastic environment carrying a moving harmonic mass. *Appl. Math. Model.* **72**, 129–154 (2019)
91. Zhang, Q., Liu, H.: On the dynamic response of porous functionally graded microbeam under moving load. *Int. J. Eng. Sci.* **153**, 103317 (2020)
92. Liu, H., Zhang, Q., Ma, J.: Thermo-mechanical dynamics of two-dimensional FG microbeam subjected to a moving harmonic load. *Acta Astronaut.* **178**, 681–692 (2021)
93. Attia, M.A., Melaibari, A., Shanab, R.A., Eltaher, M.: Dynamic analysis of sigmoid bidirectional FG microbeams under moving load and thermal load: analytical Laplace solution. *Mathematics* **10**, 4797 (2022)
94. Attia, M.A., Shanab, R.A.: On the dynamic response of bi-directional functionally graded nanobeams under moving harmonic load accounting for surface effect. *Acta Mech* **233**, 3291–3317 (2022)
95. Reddy, N.: A simple higher-order theory for laminated composite plates. *ASME J. Appl. Mech.* **51**, 745–752 (1984)
96. Attia, M.A., Mahmoud, F.F.: Size-dependent behavior of viscoelastic nanoplates incorporating surface energy and microstructure effects. *Int. J. Mech. Sci.* **123**, 117–132 (2017)
97. Attia, M.A., Mahmoud, F.F.: Modeling and analysis of nanobeams based on nonlocal-couple stress elasticity and surface energy theories. *Int. J. Mech. Sci.* **105**, 126–134 (2016)
98. Gao, X.-L., Zhang, G.: A microstructure-and surface energy-dependent third-order shear deformation beam model. *Z. Angew. Math. Phys.* **66**, 1871–1894 (2015)
99. Zhang, G., Gao, X.-L.: Elastic wave propagation in a periodic composite plate structure: band gaps incorporating microstructure, surface energy and foundation effects. *J. Mech. Mater. Struct.* **14**, 219–236 (2019)
100. Newmark, N.M.: A method of computation for structural dynamics. *J. Eng. Mech. Div.* **85**, 67–94 (1959)
101. Mathews, J.H., Fink, K.D.: Numerical methods using MATLAB, Pearson Prentice Hall Upper Saddle River, NJ.

102. Abu-Hilal, M., Mohsen, M.: Vibration of beams with general boundary conditions due to a moving harmonic load. *J. Sound Vib.* **232**(4), 703–717 (2000)
103. Shafiei, N., Mirjavadi, S.S., MohaselAfshari, B., Rabby, S., Kazemi, M.: Vibration of two-dimensional imperfect functionally graded (2D-FG) porous nano-/micro-beams. *Comput. Methods Appl. Mech. Eng.* **322**, 615–632 (2017)
104. Ansari, R., Gholami, R.: Size-dependent modeling of the free vibration characteristics of postbuckled third-order shear deformable rectangular nanoplates based on the surface stress elasticity theory. *Compos. B Eng.* **95**, 301–316 (2016)
105. Al-Basyouni, K., Tounsi, A., Mahmoud, S.: Size dependent bending and vibration analysis of functionally graded micro beams based on modified couple stress theory and neutral surface position. *Compos. Struct.* **125**, 621–630 (2015)
106. Olsson, M.: On the fundamental moving load problem. *J. Sound Vib.* **145**, 299–307 (1991)
107. Dimitrovová, Z., Varandas, J.: Critical velocity of a load moving on a beam with a sudden change of foundation stiffness: applications to high-speed trains. *Comput. Struct.* **87**, 1224–1232 (2009)

**Publisher's Note** Springer Nature remains neutral with regard to jurisdictional claims in published maps and institutional affiliations.